The Astrophysical Journal, 817:86 (18pp), 2016 February 1 doi:10.3847/0004-637X/817/2/86

STAR-FORMING BRIGHTEST CLUSTER GALAXIES AT $0.25 < z < 1.25$: A TRANSITIONING FUEL SUPPLY

M. McDonald[1], B. Stalder[2], M. Bayliss[3,4], S. W. Allen[5,6,7], D. E. Applegate[8], M. L. N. Ashby[3], M. Bautz[1], B. A. Benson[9,10,11], L. E. Bleem[10,12,13], M. Brodwin[14], J. E. Carlstrom[10,11,12,13,15], I. Chiu[16], S. Desai[16,17], A. H. Gonzalez[18], J. Hlavacek-Larrondo[19], W. L. Holzapfel[20], D. P. Marrone[21], E. D. Miller[1], C. L. Reichardt[22], B. R. Saliwanchik[23], A. Saro[16], T. Schrabback[8], S. A. Stanford[24], A. A. Stark[3], J. D. Vieira[25], and A. Zenteno[26]

[1] Kavli Institute for Astrophysics and Space Research, Massachusetts Institute of Technology, 77 Massachusetts Avenue, Cambridge, MA 02139, USA; mcdonald@space.mit.edu
[2] Institute for Astronomy (IFA), University of Hawaii, 2680 Woodlawn Drive, HI 96822, USA
[3] Harvard-Smithsonian Center for Astrophysics, 60 Garden Street, Cambridge, MA 02138, USA
[4] Department of Physics, Harvard University, 17 Oxford Street, Cambridge, MA 02138, USA
[5] Kavli Institute for Particle Astrophysics and Cosmology, Stanford University, 452 Lomita Mall, Stanford, CA 94305, USA
[6] Department of Physics, Stanford University, 382 Via Pueblo Mall, Stanford, CA 94305, USA
[7] SLAC National Accelerator Laboratory, 2575 Sand Hill Road, Menlo Park, CA 94025, USA
[8] Argelander-Institut für Astronomie, Auf dem Hügel 71, D-53121 Bonn, Germany
[9] Fermi National Accelerator Laboratory, Batavia, IL 60510-0500, USA
[10] Kavli Institute for Cosmological Physics, University of Chicago, 5640 South Ellis Avenue, Chicago, IL 60637, USA
[11] Department of Astronomy and Astrophysics, University of Chicago, 5640 South Ellis Avenue, Chicago, IL 60637, USA
[12] Argonne National Laboratory, 9700 S. Cass Avenue, Argonne, IL 60439, USA
[13] Department of Physics, University of Chicago, 5640 South Ellis Avenue, Chicago, IL 60637, USA
[14] Department of Physics and Astronomy, University of Missouri, 5110 Rockhill Road, Kansas City, MO 64110, USA
[15] Enrico Fermi Institute, University of Chicago, 5640 South Ellis Avenue, Chicago, IL 60637, USA
[16] Department of Physics, Ludwig-Maximilians-Universität, Scheinerstr. 1, D-81679 München, Germany
[17] Excellence Cluster Universe, Boltzmannstr. 2, D-85748 Garching, Germany
[18] Department of Astronomy, University of Florida, Gainesville, FL 32611, USA
[19] Département de Physique, Université de Montréal, C.P. 6128, Succ. Centre-Ville, Montréal, Québec H3C 3J7, Canada
[20] Department of Physics, University of California, Berkeley, CA 94720, USA
[21] Steward Observatory, University of Arizona, 933 North Cherry Avenue, Tucson, AZ 85721, USA
[22] School of Physics, University of Melbourne, Parkville, VIC 3010, Australia
[23] Physics Department, Center for Education and Research in Cosmology and Astrophysics, Case Western Reserve University, Cleveland, OH 44106, USA
[24] Department of Physics, University of California, One Shields Avenue, Davis, CA 95616, USA
[25] Department of Astronomy and Department of Physics, University of Illinois, 1002 West Green St., Urbana, IL 61801, USA
[26] Cerro Tololo Inter-American Observatory, La Serena, Chile
Received 2015 August 13; accepted 2015 December 3; published 2016 January 22

ABSTRACT

We present a multiwavelength study of the 90 brightest cluster galaxies (BCGs) in a sample of galaxy clusters selected via the Sunyaev Zel'dovich effect by the South Pole Telescope, utilizing data from various ground- and space-based facilities. We infer the star-formation rate (SFR) for the BCG in each cluster—based on the UV and IR continuum luminosity, as well as the [O II]$\lambda\lambda$3726,3729 emission line luminosity in cases where spectroscopy is available—and find seven systems with SFR $> 100\,M_{\odot}\,\mathrm{yr}^{-1}$. We find that the BCG SFR exceeds $10\,M_{\odot}\,\mathrm{yr}^{-1}$ in 31 of 90 (34%) cases at $0.25 < z < 1.25$, compared to ~1%–5% at $z \sim 0$ from the literature. At $z \gtrsim 1$, this fraction increases to 92^{+6}_{-31}%, implying a steady decrease in the BCG SFR over the past ~9 Gyr. At low-z, we find that the specific SFR in BCGs is declining more slowly with time than for field or cluster galaxies, which is most likely due to the replenishing fuel from the cooling ICM in relaxed, cool core clusters. At $z \gtrsim 0.6$, the correlation between the cluster central entropy and BCG star formation—which is well established at $z \sim 0$—is not present. Instead, we find that the most star-forming BCGs at high-z are found in the cores of dynamically unrelaxed clusters. We use data from the *Hubble Space Telescope* to investigate the rest-frame near-UV morphology of a subsample of the most star-forming BCGs, and find complex, highly asymmetric UV morphologies on scales as large as ~50–60 kpc. The high fraction of star-forming BCGs hosted in unrelaxed, non-cool core clusters at early times suggests that the dominant mode of fueling star formation in BCGs may have recently transitioned from galaxy–galaxy interactions to ICM cooling.

Key words: galaxies: clusters: intracluster medium – galaxies: elliptical and lenticular, cD – galaxies: starburst – X-rays: galaxies: clusters

1. INTRODUCTION

One of the great mysteries in astronomy today is why $\gtrsim$90% of the baryons in the universe, which are in diffuse gas with relatively short cooling times (e.g., Shull et al. 2012), have not cooled and formed stars. This inefficient star formation manifests as a significant disagreement between the predicted galaxy luminosity function from ΛCDM cosmological simulations and that observed in the local universe. In the most massive galaxies in the universe, which are found at the centers of rich galaxy clusters, this disagreement is maximized, with central cluster galaxies being substantially less massive than predicted by simple models (see review by Silk & Mamon 2012). This has become known as the "cooling flow problem" and can be stated simply as: "Why, given the short cooling time of the intracluster medium in the cores of some galaxy clusters, do

we not observe massive starburst galaxies at the centers of these clusters?"

Over the past couple decades, much effort has been devoted to answering this question. Early work focused on searching for multiphase gas and star formation in brightest cluster galaxies (BCGs). Numerous studies have found evidence for ultraviolet (UV) and infrared (IR) continuum (e.g., McNamara & O'Connell 1989; Hicks & Mushotzky 2005; O'Dea et al. 2008; McDonald et al. 2011b; Hoffer et al. 2012; Rawle et al. 2012; Fraser-McKelvie et al. 2014; Donahue et al. 2015), warm, ionized gas (e.g., Hu et al. 1985; Johnstone et al. 1987; Heckman et al. 1989; Crawford et al. 1999; Edwards et al. 2007; Hatch et al. 2007; McDonald et al. 2010, 2011a), and both warm and cold molecular gas (e.g., Jaffe & Bremer 1997; Donahue et al. 2000; Edge 2001; Edge et al. 2002; Edge & Frayer 2003; Salomé & Combes 2003; Hatch et al. 2005; Jaffe et al. 2005; Johnstone et al. 2007; Oonk et al. 2010; McDonald et al. 2012c)—all of which are indicative of ongoing or recent star formation. Star-forming BCGs were found preferentially in galaxy clusters with "cool cores," as identified by a central density enhancement in the ICM (e.g., Vikhlinin et al. 2007; Santos et al. 2008; Hudson et al. 2010) or low central entropy/cooling time (e.g., Cavagnolo et al. 2008, 2009; Hudson et al. 2010). These and other works established a link between the cooling ICM and the presence of multiphase gas, suggesting that cooling flows may indeed be fueling star formation in BCGs. However, the typical star-formation rates (SFRs) inferred from a variety of indicators were found to be only ∼1% of the expected ICM cooling rate (e.g., O'Dea et al. 2008). Roughly one of the two orders of magnitude in this disagreement can be accounted for by inefficient star formation (McDonald et al. 2014b), however a further order-of-magnitude disagreement between the cooling predictions and observations still remains.

Some form of feedback is necessary to prevent the bulk (∼90%) of the cooling ICM from becoming fuel for star formation. The leading candidate is "radio-mode" feedback (see reviews by Fabian 2012; McNamara & Nulsen 2012) from active galactic nuclei (AGNs), which are ubiquitous at the centers of cool core clusters (Sun 2009). The mechanical energy output from these AGN are sufficient to offset cooling on large scales, preventing runaway cooling in the majority of clusters (e.g., Bîrzan et al. 2004; Rafferty et al. 2008; Hlavacek-Larrondo et al. 2012, 2015), with a few notable exceptions (McNamara et al. 2006; McDonald et al. 2012a). The low levels of star formation and gas in multiphase filaments are understood to be local thermodynamic instabilities (e.g., Sharma et al. 2010; Gaspari et al. 2012; McCourt et al. 2012; Gaspari et al. 2015; Voit & Donahue 2015) in regions where, *locally*, cooling dominates over feedback, despite the overall global balance. These SFRs, which average a few $M_{\odot}\,\mathrm{yr}^{-1}$, may contribute a few percent to the total stellar mass of the BCG over the past ∼8 Gyr—the majority of the growth in these systems likely comes from "dry mergers" (mergers of gas-poor galaxies), which increase the stellar mass by a factor of ∼2 from $z = 1$ to $z = 0$ (Ruszkowski & Springel 2009).

The picture presented here is based almost entirely on observations of nearby ($z \lesssim 0.3$) galaxy clusters. This is, in part, due to the fact that these clusters are more easily studied because of their proximity (improved signal to noise, angular resolution, etc.). Equally important, however, is the scarcity of well-understood samples of high redshift galaxy clusters. Until recently there were few samples of galaxy clusters with known masses at $z \gg 0.5$—surveys that did probe high redshift clusters were generally flux-limited or assembled from serendipitous detections via a heterogeneous collection of methods. With the advent of large-area mm-wave surveys utilizing the Sunyaev Zel'dovich (SZ) effect (Sunyaev & Zeldovich 1972) to detect galaxy clusters, this situation has changed dramatically over the past several years, with the latest surveys achieving nearly redshift-independent detection of clusters above a fixed mass threshold at $z \gtrsim 0.3$. Most recently, the completed 2500 deg^2 SZ survey with the South Pole Telescope (SPT; Carlstrom et al. 2011) has discovered more than 500 massive galaxy clusters, the majority of which are at $z > 0.5$ (Bleem et al. 2015). In this work, we focus on a subsample of this survey that has been targeted for X-ray follow-up (McDonald et al. 2013b) and spans a redshift range of $0.3 < z < 1.2$. The availability of optical photometry and spectroscopy for the majority of the BCGs in this sample, along with archival UV (*GALEX*) and IR (*WISE*) data, allows us to study star formation in BCGs at high redshift for a complete, mass-selected sample.

The remainder of this paper is structured as follows. In Section 2 we define the sample used in this work, and present the multiwavelength data and analysis techniques that will enable us to identify star-forming BCGs. In Section 3 we isolate the sample of star-forming BCGs and attempt to determine whether there is any evolution in their properties or the properties of their host clusters. In Section 4 we discuss these results, addressing bias and selection concerns, while trying to draw a broad picture of galaxy and galaxy cluster evolution within which these results fit. We finish in Section 5, with a brief summary of the important results of this work, and a look toward the future. Throughout this work we assume $H_0 = 70\,\mathrm{km\,s^{-1}\,Mpc^{-1}}$, $\Omega_M = 0.27$, $\Omega_\Lambda = 0.73$, and a Salpeter (1955) initial mass function (IMF).

2. DATA AND ANALYSIS

2.1. Cluster Sample and BCG Selection

The sample is initially defined to include all 83 clusters from McDonald et al. (2013b), which were selected from the SPT 2500 deg^2 survey (Bleem et al. 2015) and subsequently observed in the X-ray with the *Chandra X-ray Observatory*. To this sample, we add an additional eight clusters from Bleem et al. (2015) that have archival *Chandra* data from other sources (SPT-CLJ0106-5943, SPT-CLJ0232-4421, SPT-CLJ0235-5121, SPT-CLJ0516-5430, SPT-CLJ0522-4818, SPT-CLJ0658-5556, SPT-CLJ2011-5725, SPT-CLJ2332-5053). X-ray data products, such as central entropy (K_0), are presented for this full sample of 91 clusters in McDonald et al. (2013b)—we direct the reader there for a full description of our X-ray methodology.

For each cluster, we obtained some combination of ground-based *g*, *r*, *i*, *z* optical imaging; ground-based J, H, K near-IR imaging; and *Spitzer* IRAC 3.6 μm, 4.5 μm imaging, as described in detail in Bleem et al. (2015). These data have been used to provide optical confirmation of the SZ-selected clusters, and to estimate a photometric redshift based on the member galaxy colors. We remove from our sample all clusters for which the optical-IR follow-up was performed in ⩽2 filters, preventing a reliable fit to the stellar continuum. After this cut,

we were left with a sample of 82 clusters. From this follow-up imaging, we initially select the BCG[27] as the brightest red sequence galaxy within an aperture of R_{200} centered on the SZ peak, following Song et al. (2012). We then visually inspect each cluster and select a new BCG if one, or both, of two conditions are met: (i) there is a similarly bright galaxy that is significantly closer to the X-ray peak (29% of systems); (ii) there is a bright blue galaxy on or near the X-ray peak that was not selected due to our initial preference for red galaxies (3% of systems). Wherever possible, we use *Hubble Space Telescope* (*HST*) imaging from the SPT weak-lensing follow-up programs with IDs 12246, 12477, 13412 (PIs: Stubbs, High, Schrabback) to aid in the visual identification of the BCG.

In all cases where it was not clear which galaxy was the BCG, we retain the original red BCG, allowing for two BCGs in these clusters. In this case, we give each BCG a 50% weight when performing statistical analysis, and include the limiting cases in our error estimates (i.e., upper limit contains star-forming BCG, lower limit contains passive BCG). This procedure resulted in a sample of 90 BCGs in 82 clusters. The net effect of allowing multiple BCGs in cases where the identification of a single object was challenging is to increase our uncertainties, increasing the likelihood that the "true" answer lies without our error bars.

2.2. X-Ray Analysis: Central Entropy and Luminosity

Several studies have found correlations between the amount of star formation in the BCG and the core entropy (e.g., Cavagnolo et al. 2008; O'Dea et al. 2008; Voit et al. 2015) and luminosity-derived cooling rate (e.g., Crawford et al. 1999; O'Dea et al. 2008; McDonald et al. 2010, 2011b). This has led to the conclusion that star formation is fueled in the BCG by residual cooling flows (Voigt & Fabian 2004; Tremblay et al. 2012; McDonald et al. 2014b). In order to test whether this trend was established at high-z, we require estimates of the core entropy and cooling rate for each cluster. Given that we only have ∼2000 X-ray counts per cluster, modeling the central entropy (e.g., Cavagnolo et al. 2009) or estimating the spectroscopically derived cooling rate (e.g., Voigt & Fabian 2004) is not feasible. Instead, we compute spectroscopic quantities (bolometric luminosity, temperature) from a circular aperture with a radius of $0.075\,R_{500}$ (where R_{500} was derived based on the Y_X–M_{500} relation of Vikhlinin et al. 2009), which should roughly correspond to the deprojected core temperature (see e.g., McDonald et al. 2014a). X-ray spectra extracted from this aperture are modeled with a photometric absorption (PHABS) and plasma (APEC) model, allowing the temperature, metallicity, and normalization of the plasma model to vary. This choice of aperture is meant to capture the "core" properties, reflecting the realistic fuel reservoir that the BCG may have access to.

The "central" density is computed based on the deprojected X-ray surface brightness profile, following Vikhlinin et al. (2006) and McDonald et al. (2013b). Because the measurement of electron density requires far fewer X-ray counts than the measurement of spectroscopic temperature, the central density is measured at $r = 0.01\,R_{500}$, or roughly 10 kpc for a typical cluster in this sample. We combine the projected core temperature and deprojected core density to arrive at a pseudo-deprojected core entropy ($K_0 = kT_{0.075R_{500}}\,n_{e,0.01R_{500}}^{-2/3}$). By measuring the "central" entropy within a fixed aperture (relative to the overall cluster size) at all redshifts, we avoid any issues of clusters appearing "coarser" at ever-increasing redshifts.

Unlike our previous work (McDonald et al. 2013b), here we measure "central" quantities at the X-ray peak, rather than the large-scale centroid. In general, the BCG is located closer to the X-ray peak than the centroid in cases of merging clusters, which motivated this choice. We discuss the effects of this choice in later sections. For a more detailed description of our X-ray analysis techniques, we direct the reader to McDonald et al. (2013b, 2014a).

2.3. UV–Optical–IR Photometry and Spectral Energy Distribution (SED) Modeling

Ground-based optical and/or near-infrared imaging for all clusters in this sample have been obtained at a variety of wavelengths as part of a confirmation and photometric redshift follow-up campaign. The acquisition, reduction, and calibration of these data are presented in detail in Song et al. (2012) and Bleem et al. (2015). Aperture photometry for the BCG was obtained from SExtractor (Bertin & Arnouts 1996), following Song et al. (2012) and Bleem et al. (2015).

In addition to these existing data, we acquired new ground-based u-band imaging with Megacam (McLeod et al. 2015) on the Magellan Clay telescope for 49 clusters in this sample. These 49 clusters were those that had the least restrictive upper limits on the BCG SFR at other wavelengths, generally lacking in spectroscopic or deep *GALEX* coverage. The exposure time for these observations was chosen to provide an overall sensitivity of our survey to obscured SFRs of $\sim 10\ M_\odot\ \mathrm{yr}^{-1}$; without these additional data, our sensitivity limit would vary significantly with redshift. These data were reduced using the standard photometric pipeline described in Bleem et al. (2015).

The position of each BCG was cross-referenced with the *GALEX*[28] (Morrissey et al. 2007) and *WISE*[29] (Wright et al. 2010) archives, assuming a maximum offset of 2″, from which we obtained near-UV (NUV) and near—mid IR (NIR, MIR) photometry for each BCG. If the BCG was undetected by either of these surveys, we instead obtained upper limits. *Spitzer* 3.6 μm, 4.5 μm, and *WISE* 4-band photometry was converted from Vega to AB magnitudes following Price et al. (2004). The resulting UV–optical–IR SEDs, which span 2000 Å to 22 μm in the observed frame, are shown in Figure 11 for our sample of 90 BCGs. As mentioned above, we discarded all BCGs for which we have $\leqslant 2$ photometric measurements (excluding upper limits).

The observed SEDs are fit in two stages. First, we model the full SED with a single-age population with formation redshift z_f, solar metallicity, and a IMF (Salpeter 1955). We assume a uniformly distributed range of z_f from 2 to 5 in our models, which leads to some uncertainty in our resulting stellar masses and SFRs. The spectrum for this old stellar population was generated using STARBURST99 (Leitherer et al. 1999) and was convolved with our broadband filter set. The model spectrum was fit to the data using MPFITFUN,[30] which minimizes χ^2 with respect to the two free parameters (normalization, redshift). The

[27] We note here that the term "BCG" is largely inappropriate for this work, because there may be brighter galaxies within the virial radius (e.g., AGN). The more appropriate monicker would be "central cluster galaxy," but we opt for BCG throughout this paper because it is more commonly used.

[28] http://galex.stsci.edu/GR6/

[29] http://irsa.ipac.caltech.edu/Missions/wise.html

[30] http://www.physics.wisc.edu/~craigm/idl/down/mpfitfun.pro

redshift was allowed to vary within the measured uncertainty from Bleem et al. (2015), while the normalization, which corresponds to the stellar mass of the old population, was left free.

Beyond this single-component model, we also consider additional components in the UV and IR, representing contributions from a young stellar population and warm dust, respectively. At short wavelengths, we model excess emission using Starburst99, assuming a constant SFR over the past 30 Myr (roughly the AGN duty cycle). We note that adjusting this timescale down to 10 Myr or up to 100 Myr results in deviations in the derived SFR of ∼20%. We assume that the emission from young stars is obscured by dust, incorporating the Calzetti et al. (2000) extinction law and an intrinsic reddening of $E(B-V) = 0.3 \pm 0.1$—this range is based on observations of nearby star-forming BCGs (Crawford et al. 1999; McDonald et al. 2012b). The young stellar component has a single free parameter, corresponding to the ongoing, extinction-corrected SFR. At long wavelengths, we mimic a dusty component with a mid-infrared power law ($F_\nu \propto \lambda^{2.0\pm0.5}$), following Casey (2012). This dust component is artificially truncated at shorter wavelengths, so that it will not add UV flux. We only include the young and dusty components if their inclusion improves the $\chi^2_{\rm dof}$, which is the case for 34% (31/90) of the BCGs in our sample. For the remaining 66% (59/90), the "passive-evolution" model yields a suitable fit to the data. The results of this SED fitting are shown in Figure 11.

2.4. Optical Spectroscopy

For 36 of the 95 BCGs in this sample, we have optical spectroscopy from a combination of the IMACS (Dressler et al. 2011) and LDSS3 spectrographs on *Magellan*. These spectra were initially obtained as part of a spectroscopic redshift campaign that targeted, primarily, red sequence galaxies. The full details of this spectroscopic follow-up are provided in Ruel et al. (2014) and Bleem et al. (2015). For each spectrum, we measure the [O II] and Hδ equivalent widths and the 4000 Å break strength (D_{4000}), via indices defined by Balogh et al. (1999). [O II] equivalent widths are converted to emission line fluxes using the continuum level, as determined by the SED modeling described in Section 2.2, at rest-frame 3727Å. From these 36 spectra we find significant ($>3\sigma$) [O II] emission in five systems, one of which is the Phoenix cluster (McDonald et al. 2012a). This system allows us an opportunity to compare the index-based measurement of [O II] to the total flux from deep integral field spectroscopy (McDonald et al. 2014c). Using the long-slit data, the index-based technique of Balogh et al. (1999) combined with our best-fit optical SED yields a line flux of $f_{\rm [O\,II]} = 2.2 \times 10^{-14}$ erg s^{-1} cm^{-2} for the central galaxy in the Phoenix cluster, while the total measured flux from McDonald et al. (2013a) is $f_{\rm [O\,II]} = 1.6 \times 10^{-14}$ erg s^{-1} cm^{-2}. Thus, for this single comparison, the index-based approach does an adequate job of reproducing the measurement made via emission line modeling of significantly higher-quality data.

When correcting the [O II] emission line flux for extinction, we assume that the ionized gas has a factor of two higher reddening than the stellar continuum, following Calzetti et al. (2000) and Calzetti (2001). This assumption is motivated by the idea that the warm ionized gas traces the highly ionizing O and B stars, which tend to be embedded in dusty, star-forming regions.

2.5. SFRs and Their Uncertainties

2.5.1. UV-derived SFRs

The calculation of SFRs from the UV photometry is straightforward. In Section 2.3 we describe our SED-fitting procedure, which includes an intrinsically reddened, continuously star-forming population derived from Starburst99 models. The normalization of this component yields the current SFR, under the assumption of constant star formation for the past 30 Myr.

The uncertainty in the UV-derived SFR is dominated by our uncertainty in the amount of intrinsic extinction ($E(B-V)$) and, to a lesser extent, the formation redshift of the old stellar population (z_f). In order to propagate our uncertainty in these quantities to our estimate of the SFR, we perform 100 fits to each SED, varying z_f and $E\,(B-V)$ in each fit. We assume a normal distribution for $E(B-V)$, with $E(B-V) = 0.3 \pm 0.1$, motivated by observations of nearby star-forming BCGs (Crawford et al. 1999; McDonald et al. 2012b). For the old stellar population, we assume a uniform distribution of formation epochs, from $z_f = 2.0$ to 5.0 Gyr. This Monte-Carlo approach results in typical uncertainties in the UV-derived SFRs of 0.38 dex, or a factor of ∼2.5.

2.5.2. [O II]-derived SFRs

As described in Section 2.3, [O II] fluxes are derived from a combination of indices (Balogh et al. 1999), which provide an estimate of the equivalent line width, and SED fitting, which provides the interpolated continuum level at 3727 Å. We convert the measured emission line flux to an SFR, assuming that the $\rm SFR_{[O\,II]} = 9.53 \times 10^{-42}\ L_{[O\,II]}$ (Kewley et al. 2004). As in Section 2.5.1, we assume a normal distribution of intrinsic reddening, with $E\,(B-V)_{\rm gas} = 2E\,(B-V)_{\rm stars}$, following Calzetti et al. (2000) and Calzetti (2001). As is the case for the UV-derived SFRs, our uncertainty in this extinction correction dominates the uncertainty in the inferred SFR. Propagating this uncertainty through the fitting procedure via a Monte-Carlo approach yields typical uncertainties of 0.19 dex, or a factor of ∼1.5.

2.5.3. IR-derived SFRs

In the mid-infrared, we derive the SFR by first extrapolating our power-law fit from observed 22 μm to rest-frame 24 μm. The uncertainty on this calculation is both redshift dependent, because at higher redshift we are extrapolating over a larger wavelength range, and dependent on the assumed power-law slope. We incorporate the uncertainty in the power-law slope ($\alpha = 2.0 \pm 0.5$; Casey 2012) in our calculation of the 24 μm luminosity by assuming a normal distribution of values and performing 100 fits to the data. The average resulting uncertainty in $L_{24\,\mu m}$ is 0.2 dex, or a factor of ∼1.6. These extrapolated values of $L_{24\,\mu m}$ are then converted into an estimate of the SFR, following Calzetti et al. (2007).

2.5.4. Comparison of SFR Estimates

In Figure 1, we compare SFRs derived from the three indicators described above. We have limited overlap between the three subsamples, with only three BCGs having both IR- and UV-derived SFRs and an additional four BCGs with both UV- and [O II]-derived SFRs. Only a single BCG (SPT-CLJ2344-4243) has SFRs inferred from all three methods.

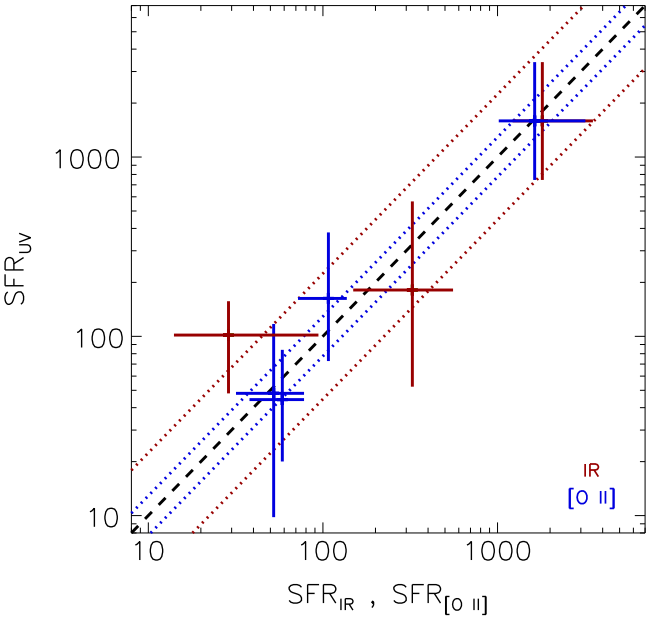

Figure 1. Comparison of SFRs derived via UV, [O II], and IR relations for all six systems with multiple measurements. The dashed line represents the one-to-one relation, while the dotted lines show the measured scatter between the UV–IR (red) and UV–[O II] (blue) relations. The dominant source of uncertainty for UV- and [O II]-derived SFRs is the extinction correction, while for IR it is the extrapolation from observed frame 22 μm to rest-frame 24 μm. This figure demonstrates the overall agreement between these different indicators, despite the significant uncertainties involved in estimating the SFR.

Nonetheless, we proceed to compare how well these estimates agree for systems in common. In general, SFR estimates from different indicators agree within the systematic errors. Assuming a one-to-one relation, we measure a scatter of 0.37 dex between UV- and IR-derived SFRs, and 0.15 dex between UV- and [O II]-derived SFRs. The better agreement between the UV- and [O II]-derived SFRs is most likely due to the fact that the dominant systematic uncertainties (extinction, old stellar population age) are correlated between these SFR estimates. SFRs for each BCG are listed in Table 2, along with relevant information about the host cluster.

2.6. AGN Contamination

Before presenting results from this survey, we would like to draw attention to one potential issue with our approach: All three indicators of star formation employed here—UV continuum, [O II] line emission, and IR continuum—are also indicators of active nuclei. The relative amounts of contamination at each of these wavelengths depends on the type of AGN considered. For example, in the Phoenix cluster, more than half of the total IR continuum comes from a dusty QSO. On the other hand, this AGN contributes <5% to the UV and [O II] emission. Several of the SEDs shown in Figure 11 exhibit a power-law shape that is consistent with both a dusty starburst and an AGN.

In an attempt to quantify the contamination due to AGN in this sample, we consider in Figure 2 the 3.5–4.5 μm color for 49 BCGs with *Spitzer* data and 82 BCGs with *WISE* data. Color corrections from Stern et al. (2012) have been applied to match data from these telescopes to a common photometric system. Following Stern et al. (2005, 2012), we classify systems with mid-IR colors [3.5]−[4.5] > 0 as AGN, while

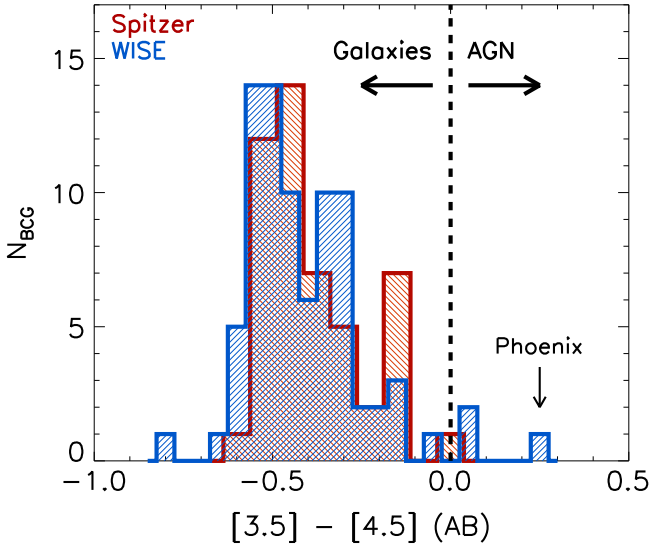

Figure 2. Distribution of mid-IR color, [3.5]–[4.5], for the BCGs in this study from the *Spitzer* (red) and *WISE* (blue) space telescopes. The vertical cut at [3.5]–[4.5] = 0, which separates galaxies from AGN, is motivated by Stern et al. (2005) and is valid for systems at $z \lesssim 1.3$. This figure demonstrates that, with the exception of the Phoenix cluster (SPT-CLJ2344-4243), this sample of BCGs is relatively free of strong AGN.

those with redder colors are either passive or star-forming galaxies. In this color space, the Phoenix cluster (McDonald et al. 2012a) is the only BCG harboring a strong AGN. At most, we estimate that ∼four clusters in this sample may harbor strong AGN at their centers, based on this mid-IR color selection. This lack of AGN contamination is further confirmed by visual inspection of the *Chandra* data for each cluster, which show a general lack of strong X-ray point sources coincident with the BCG in all clusters, with the exception of Phoenix.

We proceed with this work assuming that all systems identified as star forming are, indeed, star forming, but remain cognizant of the fact that some fraction of these may host an AGN. We return to this dilemma in the discussion section.

3. RESULTS

Below, we summarize the key results to emerge from this data set. We defer a detailed discussion of these results to the discussion section.

3.1. SFRs in BCGs at $0.25 < z < 1.2$

In Figure 3 we show the SFRs, derived via three different methods, for the sample of BCGs described in Section 2.1. This plot demonstrates that the *WISE* mid-IR data typically provide the best upper limits at low-redshift, but are unable to provide meaningful upper limits on the SFR for BCGs at $z \gtrsim 0.5$. At $z > 0.5$, the most restrictive limit generally comes from our deep u-band follow-up program, which was designed to achieve a redshift-independent sensitivity. For the most part, we are sensitive to SFRs higher than 10 $M_{\odot}\,\mathrm{yr}^{-1}$, with <10% of systems having limits higher than this threshold.

In the right panel of Figure 3, we combine the constraints from the three different SF indicators. This plot shows a significant number of BCGs, with SFRs from 10 to 300 $M_{\odot}\,\mathrm{yr}^{-1}$ at $z > 0.4$. One quarter (7/31) of the star-forming BCGs have SFR > 100 $M_{\odot}\,\mathrm{yr}^{-1}$—of these, five are at $z > 0.9$.

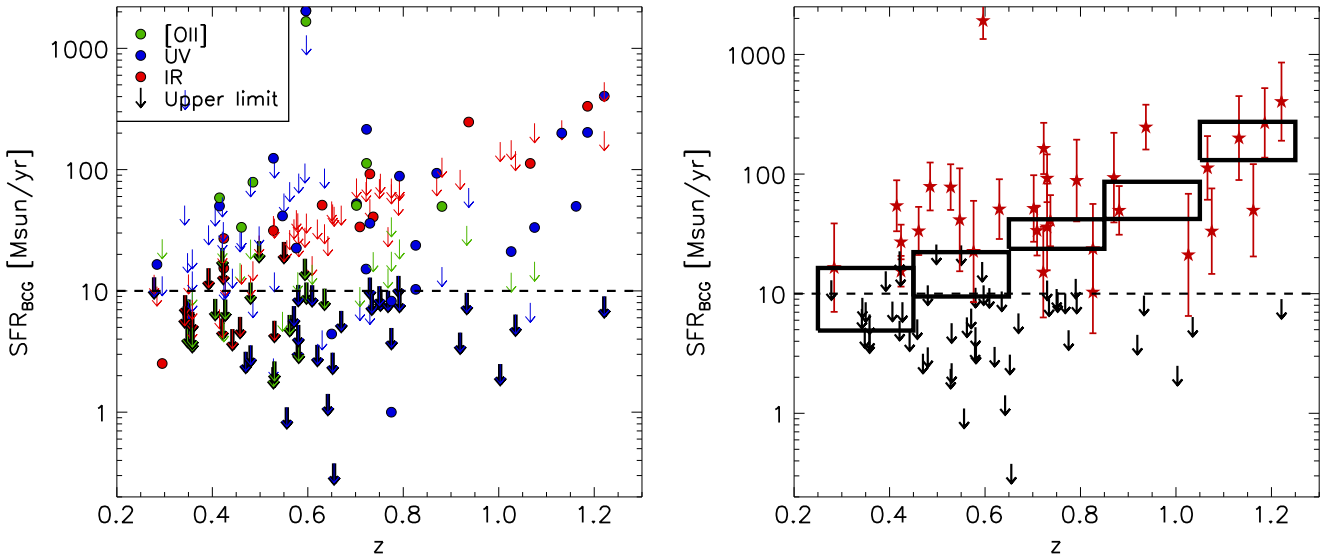

Figure 3. Left: measured star-formation rates (filled circles) and upper limits (arrows) for the BCGs in this sample as a function of redshift. We show individual measurements from each method (UV continuum, IR continuum, [O II] emission line) where available. The horizontal dashed line represents our cutoff depth of SFR $= 10\ M_{\odot}\ \mathrm{yr}^{-1}$. We highlight the most restrictive upper limit for each BCG with a black outline, showing that the best constraints at high-z come from deep rest-frame UV imaging, while at low-z archival data from *WISE* is able to provide robust upper limits. Right: similar to left panel, but now showing only the most constraining upper limit or detection (red) for each BCG. Where multiple SFRs were measured for a given cluster (see Figure 1), we take the average. Systematic uncertainties (see Section 2.5) are shown as vertical error bars. For UV- and [O II]-based SFRs, the uncertainty is dominated by the extinction correction, while for IR-based SFRs the uncertainty is dominated by the extrapolation of the observed 22 μm to rest-frame 24 μm. Black rectangles show the average SFR in different redshift bins, where the height represents the combined statistical uncertainty in the mean and additional uncertainty due to non-detections.

For comparison, prior to this work there were only four confirmed clusters with extinction-corrected SFR $> 100\ M_{\odot}\ \mathrm{yr}^{-1}$ in their BCG: Abell 1835 (McNamara et al. 2006), RX J1504.1-0248 (Ogrean et al. 2010), MACS J1931.8-2634 (Ehlert et al. 2011), and the Phoenix cluster (McDonald et al. 2012a). The median SFR for the 31 star-forming BCGs identified over the full redshift range is $50\ M_{\odot}\ \mathrm{yr}^{-1}$. It is worth noting that five of the seven most star-forming BCGs (SFR $> 100\ M_{\odot}\ \mathrm{yr}^{-1}$) are at $z \geqslant 0.9$, despite the fact that only 15% of the clusters in this sample are at such high redshift. Likewise, three of the most star-forming BCGs are at $z > 1.1$, despite this representing 6% of the sample.

We also show the average SFR as a function of redshift in five redshift bins, in the right panel of Figure 3. These averages, provided in Table 1, have uncertainties that are derived by bootstrapping errors on individual data points. For non-detections, we assume zero SFR for the lower-bound of the uncertainty and the upper limit for the upper bound. Thus, the ranges shown encompass both the statistical uncertainty in the mean from detections and the uncertainty in the true value of the non-detections. This analysis reveals a strong evolution in the average SFR in BCGs over the past nine Gyr. This increase in the average SFR is driven largely by a decrease in the number of non-detections at high-z, which we discuss next.

3.2. The Evolving Fraction of Star-forming BCGs

In Figure 4 we show how the fraction of BCGs with SFR $> 10\ M_{\odot}\ \mathrm{yr}^{-1}$ (hereafter f_{SF}) has evolved over time. Within the sample presented here, this fraction evolves from ~20% at $0.25 < z < 0.65$, to ~50% at $0.65 < z < 1.05$, to ~90% at $z > 1.05$. This evolution is visible in Figure 3 as a relative lack of non-detections at the highest redshifts compared to the lowest redshifts. This result indicates that the fraction of clusters harboring a starburst in their central, most massive galaxy grows by a factor of ~3 between $z \sim 0.6$ and $z \sim 1.1$.

Table 1
Average BCG Properties

z	N_{cl}	$\langle M_{*} \rangle$ ($10^{12}\ M_{\odot}$)	$\langle \mathrm{SFR} \rangle$ ($M_{\odot}\ \mathrm{yr}^{-1}$)	$\langle \mathrm{sSFR} \rangle$ (Gyr^{-1})
0.25–0.45	19	2.09	4.0–15	0.002–0.007
0.45–0.65	28	1.97	7.0–24	0.004–0.012
0.65–0.85	22	1.47	20–41	0.013–0.028
0.85–1.05	8	1.39	42–84	0.030–0.061
1.05–1.25	6	1.54	89–320	0.058–0.205

Note. Average values for BCGs in five redshift bins, as shown in Figures 3 and 5. The ranges quoted on $\langle \mathrm{SFR} \rangle$ and $\langle \mathrm{sSFR} \rangle$ correspond to the combined uncertainty in the measurements (bootstrapping errors), the uncertainty in the BCG choice, and the added uncertainty associated with stacking non-detections. The total number of clusters is less than the number of BCGs, due to the fact that we consider multiple potential BCGs for several clusters.

Even more intriguing is that, at $z \sim 0$, $f_{\mathrm{SF}} \sim 0\%$–10% (Donahue et al. 2010; Fraser-McKelvie et al. 2014), suggesting an even more dramatic decline since $z > 1$. In Figure 4, we compile estimates of f_{SF} from various surveys, spanning $0 < z < 0.6$. These surveys include both optically selected (McDonald 2011; M. McDonald et al., in preparation) and X-ray-selected (Donahue et al. 1992, 2010; Hoffer et al. 2012; Rawle et al. 2012; Fraser-McKelvie et al. 2014; Donahue et al. 2015) clusters, and are being compared here to an SZ-selected sample. For the ACCEPT (Cavagnolo et al. 2009) and CLASH (Donahue et al. 2015) samples, we apply a small correction because both of these cluster samples are biased toward cool core clusters. This bias correction assumes that the true, underlying fraction of cool core clusters is 30% (Haarsma et al. 2010; Hudson et al. 2010; McDonald et al. 2013b) and that non-cool cores do not have star-forming BCGs at $z \lesssim 0.5$ (Cavagnolo et al. 2008; O'Dea et al. 2008; McDonald et al. 2010). This well-motivated correction brings the observed

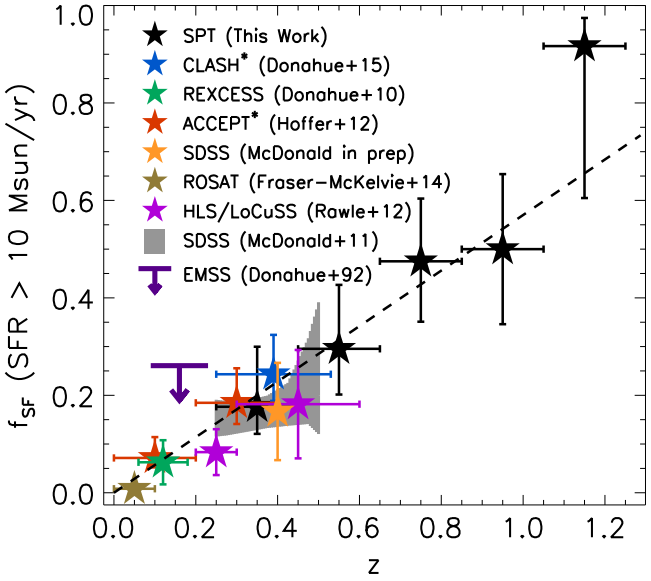

Figure 4. Fraction of BCGs with SFR $> 10\ M_{\odot}\ \mathrm{yr}^{-1}$ (f_{SF}) as a function of redshift. Black points show data from this work in four different redshift bins, while colored points show data from previous works over $0 < z < 0.6$ (Donahue et al. 1992, 2010, 2015; McDonald 2011; Hoffer et al. 2012; Rawle et al. 2012; Fraser-McKelvie et al. 2014). Samples marked with an asterisk in the legend have had a bias correction applied, assuming that non-cool cores have passively evolving BCGs and that the true underlying fraction of cool cores is 30% (see Section 3.2). This plot demonstrates consistency between a wide variety of samples based on X-ray, optical, and SZ selection. We find a steady rise in the fraction of star-forming BCGs, from $f_{\mathrm{SF}} \sim 0\%$ at $z \sim 0$ to $f_{\mathrm{SF}} \sim 70\%$ at $z \sim 1.2$. This growth is depicted with a best-fit dashed line. Vertical error bars are derived based on the methods described by Cameron (2011) for binomial populations.

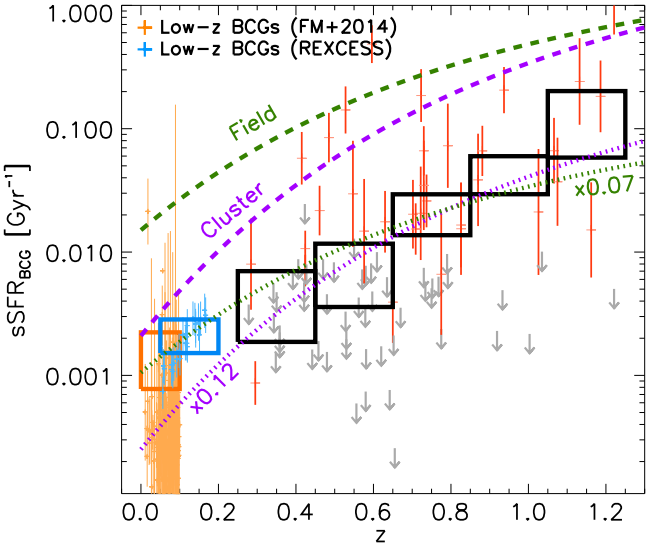

Figure 5. Specific star-formation rate (sSFR) as a function of redshift for BCGs in this work (red points, gray upper limits) and for nearby clusters (Haarsma et al. 2010; Fraser-McKelvie et al. 2014). Black boxes show the combined sSFR in different redshift bins, computed as the sum of the individual SFRs divided by the sum of stellar masses—these points include the upper limits, with the vertical size of the boxes representing the associated uncertainty (see Table 1). Dashed blue and purple curves show the evolution measured for the field and cluster environment, respectively, from Alberts et al. (2014). We show these curves, for comparison, with the BCG evolution at $0.5 \lesssim z \lesssim 1$. At low-$z$, the BCG evolution is slower than for typical cluster members, suggesting an additional source of fuel that the non-BCG cluster galaxies are not accessing, while at high-z ($z > 1$) there appears to be a rapid increase in the amount of star formation in BCGs.

value of f_{SF} in line with other, more representative samples. Encouragingly, at $z \sim 0.4$ there are five distinct measurements of f_{SF} based on three different selection methods, which all agree that the fraction of star-forming BCGs is $20 \pm 5\%$. The agreement between our measurement of f_{SF} from SPT at $0.25 < z < 0.5$ and these earlier works suggests that our methodology is sound.

We show, in Figure 4, a linear fit to the star-forming BCG fraction, f_{SF}, as a function of redshift. The best-fitting line passes through the origin and has a slope of 0.57, implying a rapid evolution in f_{SF} over the past ~9 Gyr. Such a fit is not physically well-motivated, and does not capture the rapid growth at late times. However, regardless of the choice of parametrization, it is clear from Figure 4 that the fraction of clusters harboring a strongly star-forming BCG at $z \sim 1$ is *significantly* ($>3\sigma$) higher than at $z \sim 0$. This evolution is perhaps unsurprising, because galaxies in general were more star forming at early times. To address this comparison, we next compare the BCG evolution to that observed in field galaxy and other cluster members over similar redshift intervals.

3.3. Specific SFRs of BCGs at $0.25 < z < 1.2$

When comparing BCGs to other galaxies, it is necessary to normalize by the stellar mass of the individual galaxy. For a typical BCG, with $M_{*} \sim 10^{12} M_{\odot}$, an SFR of $10\ M_{\odot}\ \mathrm{yr}^{-1}$ is negligible in terms of contributing to the overall mass of the cluster, requiring 100 Gyr to double the stellar mass. However, this same SFR in a low-mass galaxy like M82 is enough to power massive outflows and modify the galaxy morphology and stellar content on short (Myr) timescales (Förster Schreiber et al. 2003). Thus, if we want to compare BCG evolution to field galaxy evolution, we must consider instead the *specific* SFR, or sSFR, defined as $\mathrm{sSFR} \equiv \mathrm{SFR}/M_{*}$.

In Figure 5 we show the sSFR for BCGs in this work, as well as BCGs in similar-mass, low-z clusters from Haarsma et al. (2010) and Fraser-McKelvie et al. (2014). In calculating the sSFR, we use the stellar mass of the old population obtained in the SED-fitting process (see Section 2.3). For comparison, we show the average sSFR for field and cluster galaxies from Alberts et al. (2014). This earlier work showed that, at present, cluster galaxies have suppressed star formation compared to the field. However, at $z \sim 1.2$, galaxies in clusters are as star forming as their field counterparts, and are evolving more rapidly. To match the analysis of Alberts et al. (2014), who calculate sSFR(z) by stacking far-IR data on galaxy positions, we estimate average sSFR values for our data by separately summing the total SFR and total stellar mass for galaxies in five redshift bins. For BCGs with upper limits on their SFR, we assume two limiting cases: the case where the SFR is equal to the upper limit, and the case where the SFR is zero. The net result of this stacking is shown in Figure 5 and Table 1, where the height of the black boxes represents the combined uncertainty in the measurements (bootstrapping errors), the uncertainty in the BCG choice, and the added uncertainty associated with stacking non-detections.

Figure 5 demonstrates that, at $0.5 \lesssim z \lesssim 1$, BCGs are evolving similarly to the cluster member galaxies, suggesting a common fueling mechanism. At low-z ($z \lesssim 0.5$), the evolution of BCGs is less rapid than in the cluster environment, suggesting that the quenching processes acting on member

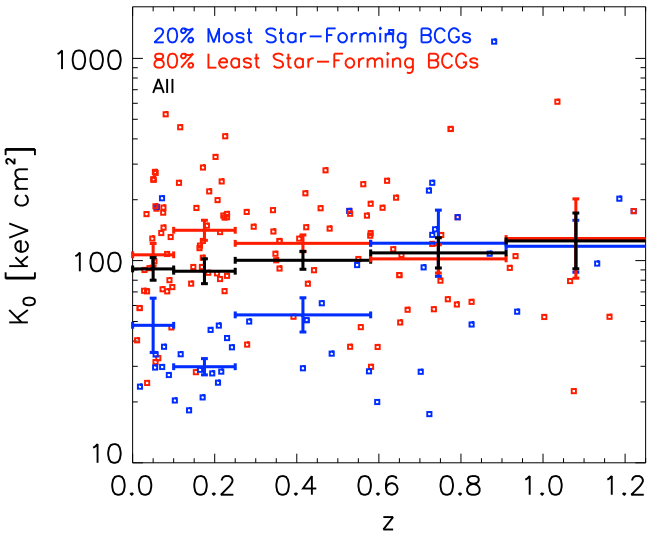

Figure 6. Cluster central entropy (K_0) as a function of redshift for all clusters in this sample (see also McDonald et al. 2013b). Here, we separate clusters into two subsamples within each redshift bin: those harboring the 20% most star-forming BCGs (blue) and those harboring the 80% least star-forming BCGs (red). At $0.0 < z < 0.25$ we show clusters from the ACCEPT database of Cavagnolo et al. (2009), where star-formation rates come from Fraser-McKelvie et al. (2014) ($z < 0.1$) and Crawford et al. (1999) ($z > 0.1$). For these low-z clusters, we show only systems with $M_{500} \geqslant 3 \times 10^{14}\,M_{\odot}$ and have recomputed the central entropy in an aperture with radius 15 kpc (corresponding to ~0.01–0.02R_{500}), to prevent resolution bias (see e.g., Panagoulia et al. 2014). In each redshift interval we show the mean K_0 and the error on the mean for both subsamples, as well as the total population (black). While at $z \lesssim 0.6$ there is a clear separation in populations, with the most star-forming BCGs being found primarily in clusters with low-entropy cores (e.g., Cavagnolo et al. 2008), there appears to be no correspondence between cool cores at star-forming BCGs at $z \gtrsim 0.6$.

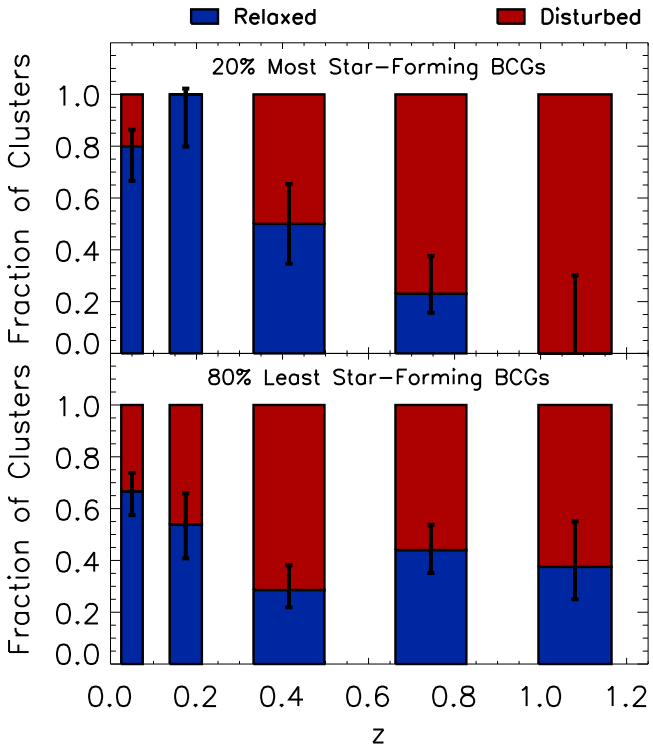

Figure 7. This plot shows the fraction of relaxed (blue) and disturbed (red) clusters as a function of redshift for two subsamples: clusters harboring the 20% most star-forming BCGs (upper panel) and those harboring the 80% least star-forming BCGs (lower panel). For low-redshift clusters ($z < 0.3$, two leftmost bins) relaxedness has been determined based on the X-ray "symmetry" reported in Mantz et al. (2015), while star-formation rates come from Fraser-McKelvie et al. (2014) and Crawford et al. (1999). For the three higher-redshift bins, relaxedness is quantified following Nurgaliev et al. (2013). This figure demonstrates that the most star-forming BCGs tend to be found in relaxed clusters at low-z, in agreement with the literature, while at high-z they are found predominantly in morphologically disturbed clusters. There is no strong trend in the the morphology of clusters hosting the 80% least star-forming BCGs.

galaxies (e.g., ram-pressure stripping, strangulation) may not be affecting the central galaxy. This change in slope may be due to the gas reservoir being replenished in BCGs by cooling of the ICM, which is likely fueling star formation in the lowest redshift BCGs (e.g., McDonald et al. 2011b). We will return to this idea in the discussion below. At $z \gtrsim 1$ there is marginal evidence that BCGs may be evolving more rapidly than the member galaxies, suggesting a preferential quenching in the cluster core.

3.4. Which Clusters Host Star-forming BCGs?

At low-z, star-forming BCGs are, with very few exceptions, found in low-entropy, relaxed "cool core" clusters (e.g., Cavagnolo et al. 2008). This appears to still be the case for CLASH clusters out to $z \sim 0.4$ (Donahue et al. 2015), and for individual clusters at higher redshift (e.g., McDonald et al. 2012a). However, it has not yet been established whether the presence of a cool core at high-z correlates with a star-forming BCG.

In Figure 6, we show the distribution of central entropy (K_0) as a function of redshift for clusters hosting the most star-forming BCGs compared to those hosting the most passive BCGs. Specifically, in each redshift bin we separately compute the average central entropy for the clusters harboring the 20% most star-forming BCGs (e.g., Perseus, Abell 1835, Phoenix, etc.) and for those harboring the 80% most passive BCGs. At $z < 0.3$, we show clusters from the ACCEPT sample (Cavagnolo et al. 2009), where the SFRs are inferred from archival infrared data ($z < 0.1$; Fraser-McKelvie et al. 2014) or the Hα line luminosity ($z > 0.1$; Crawford et al. 1999). We recomputed the central entropy in a 15 kpc aperture (~0.015R_{500}) for clusters at $z < 0.3$ to match our more coarse, high-z aperture, and to avoid resolution bias (e.g., Panagoulia et al. 2014). We only include clusters with $M_{500} > 3 \times 10^{14}\,M_{\odot}$ (based on L_X–M relation from Pratt et al. 2009) to mimic the SPT selection. We find, in agreement with previous works (Cavagnolo et al. 2008), that the clusters hosting the most star-forming BCGs have a typical central entropy of $K_0 \sim 30$ keV cm^2, while those hosting the least star-forming BCGs have $K_0 \sim 100$ keV cm^2. As the redshift increases, the average core entropy in clusters hosting the most star-forming BCGs increases to ~40 keV cm^2 ($z \sim 0.4$), and then to ~100 keV cm^2 ($z \sim 0.7$). In the two highest redshift bins ($z \gtrsim 0.6$) there is no statistical difference between the distribution of core entropy in clusters with star-forming and passive BCGs. We find no strong evolution in the core entropy of the full sample, or in the subsample of clusters with passively evolving BCGs. This seems to suggest that, while ICM cooling is likely responsible for providing the fuel for star formation in low-z clusters, a different mechanism is responsible for star formation in the high-z BCGs.

Another mechanism for forming stars in BCGs is via mergers with gas-rich galaxies. Under the assumption that such mergers happen most often shortly after the infall of a group or

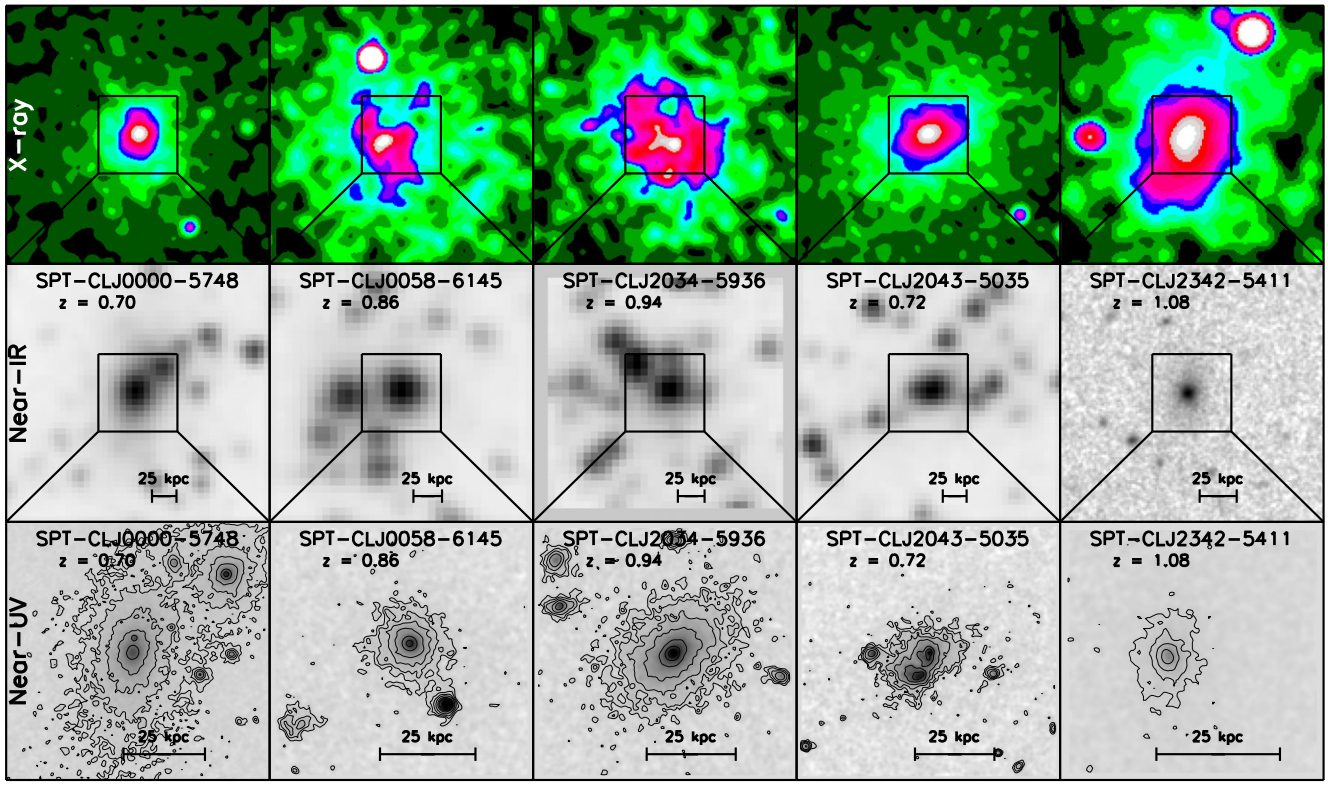

Figure 8. Upper row: smoothed X-ray images from *Chandra* of five clusters from this paper at $z > 0.7$, with rest-frame near-UV imaging from *HST* and with both relaxed X-ray morphology and a low-entropy core. The field of view for each cluster corresponds to R_{500} on a side. Middle row: near-infrared image (FourStar or *Spitzer*) of the inner region of the cluster. The footprint of this image is overlaid on the X-ray image above. In all panels, the galaxy identified as the BCG is at the center of the field of view. Lower row: rest-frame near-UV image of the BCG from *HST*. The footprint of each image is shown on the near-IR image directly above it. These images show that, for the most part, the relatively smooth UV emission in these galaxies is tracing the underlying old stellar populations, contrary to the highly asymmetric, filamentary star formation observed in the cores of low-z, relaxed galaxy clusters.

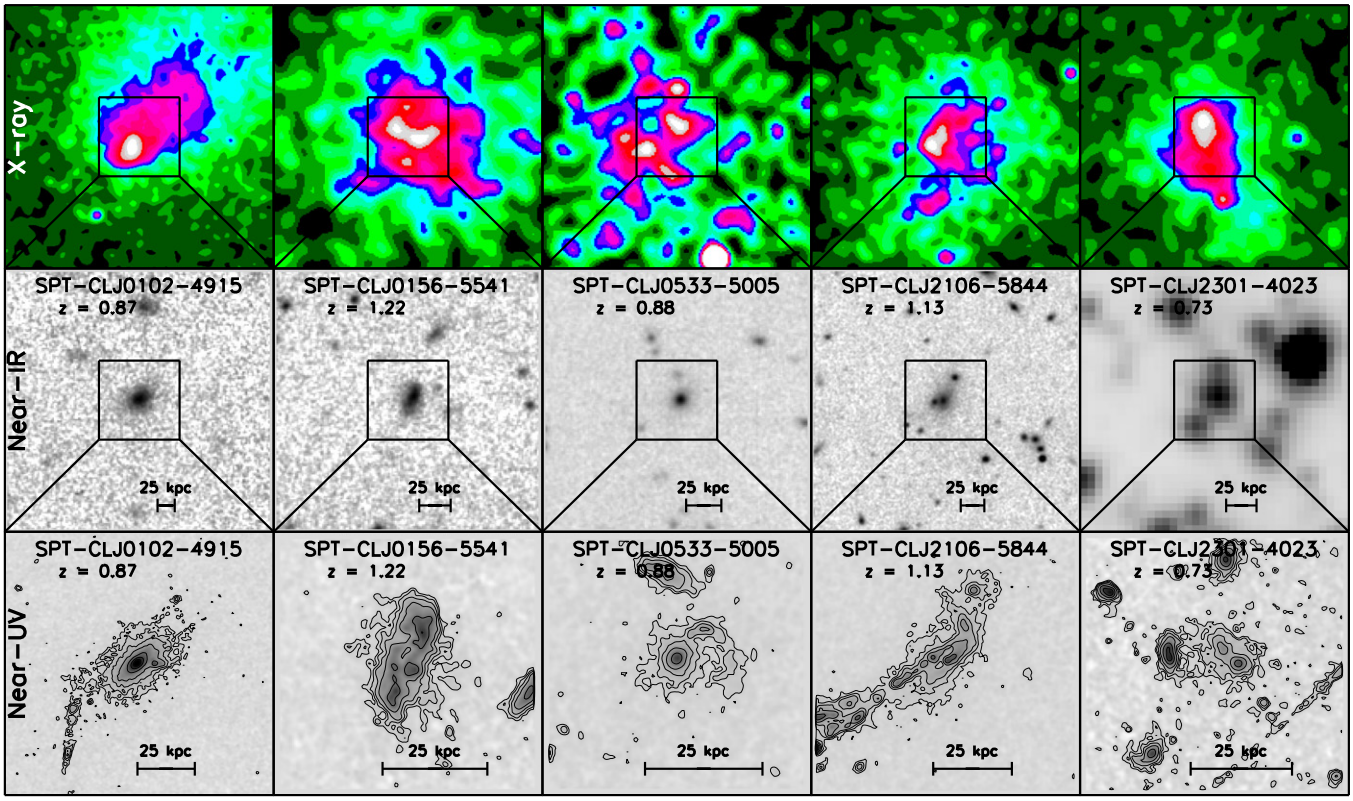

Figure 9. Similar to Figure 8, but now showing five clusters at $z > 0.7$ with disturbed X-ray morphologies. The BCGs in these clusters all have highly asymmetric UV emission, suggesting a different mode of star formation than the BCGs in relaxed clusters.

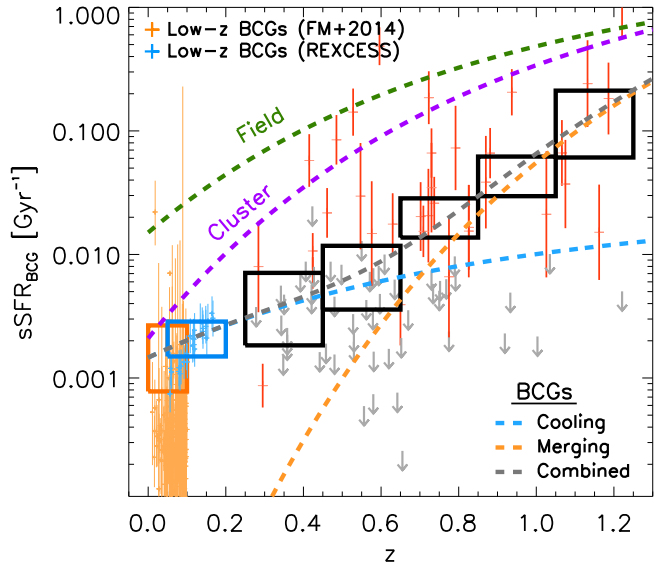

Figure 10. Here, we repeat Figure 5, but with a two-component fit to the BCG evolution. This fit assumes two epochs of star formation in BCGs: low-level star formation at present day, which correlates to the presence of a relaxed morphology and cool core in the ICM, and a rapid increase in star formation at $z \gtrsim 0.8$, which correlates to the presence of disturbed ICM morphology. We propose that this is indicative of two epochs of BCG star formation: merger-driven at early times, and cooling-induced at late times.

other massive halo, which provides an influx of new galaxies along orbits that may not be stable, we would expect BCGs with star formation being fueled by mergers to reside in clusters with disturbed X-ray morphology. In Figure 7, we test this scenario. For clusters in the SPT sample, we define X-ray morphology using the "$a_{\rm phot}$" parameter, following Nurgaliev et al. (2013), with a relaxed critereon of $a_{\rm phot} < 0.1$. This quantity is less biased to signal to noise than other indicators, such as power ratios and centroid shift, but is consistent with these in the limit of high signal to noise, as is demonstrated by Nurgaliev et al. (2013). At low-z, we use the recently compiled list of "symmetry" measurements from Mantz et al. (2015), using overlapping clusters to determine a common "relaxed" criterion. As before, for clusters at $z < 0.1$ and $0.1 < z < 0.3$, we use BCG SFRs from Fraser-McKelvie et al. (2014) and Crawford et al. (1999), respectively, cutting on mass ($M_{500} \geqslant 3 \times 10^{14} M_{\odot}$) in order to ensure uniformity in the samples.

Figure 7 confirms that, at $z < 0.3$, the most star-forming BCGs tend to reside in relaxed, cool core clusters. The star formation in these BCGs is most likely being fueled by the cooling ICM, where cooling flows are most commonly found in relaxed clusters. On the contrary, at $z \gtrsim 0.6$, the most star-forming BCGs are found in clusters with disturbed X-ray morphology, with ~90% of the most star-forming BCGs at $z \gtrsim 0.6$ being found in such systems. This implies that, at early times, star formation in the BCG is more strongly correlated with the dynamic state, rather than the cooling state, of the ICM —the inverse to what is observed in the nearby universe.

Figures 6 and 7 suggest that there is a transition from star formation in low-z BCGs being linked to low-entropy, cool core clusters, to star formation in high-z BCGs being related more to a disturbed cluster morphology than to the cooling properties of the ICM. Below we will discuss possible interpretations of this result, and others presented thus far, while also addressing any potential systematic biases in this study.

4. DISCUSSION

4.1. Comparing X-ray and UV Morphology for Individual Star-forming BCGs

Based on Figures 6 and 7, there appears to be an evolving connection between star formation in the BCG and the host cluster morphology. In order to investigate the fuel source for this star formation (i.e., cooling, gas-rich mergers, etc.), and determine whether it is linked to the dynamical state of the cluster, we require rest-frame UV imaging at significantly higher angular resolution. Fortunately, many of the high-z clusters in this sample have been observed by the *HST* as part of various weak-lensing programs (PIs: Stubbs, High, Schrabback). These observations are all in the F606W filter, which corresponds to rest-frame u-band at $z \sim 0.7$ and <3000 Å at $z > 1$. These data provide a detailed view of the young stellar populations in a subsample (10/14) of high-z star-forming BCGs.

In Figures 8 and 9, we highlight the X-ray and UV morphology of the cluster and BCG, respectively, for all 10 clusters with available rest-frame u-band (or bluer) *HST* imaging at $z > 0.7$. For each cluster, we also show a near-IR image of the core region to demonstrate that these star-forming galaxies do indeed have the highest stellar mass of all the galaxies in the core, which is consistent with being the BCG. We divided these 10 clusters by X-ray morphology into two subsamples: relaxed ($a_{\rm phot} < 0.3$ and $K_0 < 95\,{\rm keV\,cm^2}$) and unrelaxed ($a_{\rm phot} > 0.3$ or $K_0 > 95\,{\rm keV\,cm^2}$). The five most relaxed clusters (Figure 8), in general, have relatively smooth, symmetric UV morphologies that resemble the underlying old stellar (near-IR) distribution. We caution that much of this near-UV emission may originate in the old stellar populations (see e.g., Hicks et al. 2010)—we require either far-UV imaging or equally high angular resolution imaging in a near-IR band (allowing subtraction of the old population) to determine the morphology of the excess UV emission due exclusively to young stars. Two of the BCGs shown in Figure 8 (SPT-CLJ0000-5748, SPT-CLJ2043-5035) appear to be in the midst of major mergers, based on both the near-IR and near-UV imaging, despite the fact that these two BCGs reside in the two most relaxed high-z clusters in our sample. None of the star-forming BCGs in this high-z, relaxed cluster subsample show evidence for extended, asymmetric filaments of star formation, which are commonly found in analogous low-z systems (e.g., O'Dea et al. 2010; McDonald et al. 2011b; Donahue et al. 2015, Tremblay et al. 2015). Instead, the UV emission is concentrated in the BCG center for four out of five BCGs, perhaps indicating that these systems are experiencing either nuclear starbursts or are AGN misidentified as star-forming galaxies.

On the other hand, in the five least-relaxed clusters (Figure 9), the UV emission in and around the BCG is clumpy and filamentary. In particular, SPT-CLJ0102-4915 and SPT-CLJ2106-5844 exhibit clumpy UV emission extending 61 and 57 kpc from the BCG center, respectively. This is comparable to the most extended star-forming filaments found in Abell 1795 (50 kpc; McDonald & Veilleux 2009) and Perseus (60 kpc; Conselice et al. 2001; Canning et al. 2014). In all five

of these BCGs, there are a minimum of two distinct UV peaks —in several systems, the brightest UV peak is offset from the BCG nucleus. Unlike the five BCGs in the more relaxed clusters, none of these systems are consistent with being purely AGN, given their complex morphology.

While incomplete, these *HST* data suggest a qualitative difference in UV morphology between BCGs in relaxed, cool core clusters and those in unrelaxed systems. In relaxed, cool core clusters, where low-z surveys tend to find star-forming BCGs, we find (in four out of five cases) smooth, centrally concentrated UV morphologies. In the more morphologically disturbed systems (based on X-ray imaging), we find (in five out of five cases) clumpy or filamentary UV emission, with several ($\gtrsim$3) distinct emission peaks. Follow-up studies involving deep, high spatial resolution imaging at both far-UV and near-IR of a larger sample of high-z BCGs are necessary to determine whether this emerging trend is merely coincidence or evidence for a link between central star formation and the dynamical state of the cluster core.

4.2. An Evolving Fuel Supply?

The results presented in Section 3 suggest that, at high-z, the potential for star formation in the BCG is maximized when that BCG belongs to a dynamically active cluster. This is contrary to the established wisdom—based on numerous studies of low-z clusters—that the most relaxed, cool core clusters tend to harbor the most star-forming BCGs (e.g., Crawford et al. 1999; Edwards et al. 2007; Cavagnolo et al. 2008; Donahue et al. 2010). We proceed with a discussion of these results under the assumption that the X-ray morphology traces the dynamical state of the cluster, or, more specifically, that morphologically disturbed clusters in the X-ray are undergoing (or have recently undergone) a major merger.

At early times, the cores of galaxy clusters contained a higher fraction of star-forming galaxies than they do today—this is known as the "Butcher-Oemler Effect" (Butcher & Oemler 1984). This trend continues with increasing redshift, such that at $z \sim 1.4$, the SFR in the field and in the cluster environment are indistinguishable (Brodwin et al. 2013; Alberts et al. 2014; Wagner et al. 2015, see also Figure 5). Thus, we would expect there to be a significantly higher fraction of gas-rich galaxies in our high-z subsample than in the low-z systems, particularly in the inner cores where gas depletion is most effective at low-z. Regardless of the impact angle of a cluster–cluster merger (as long as it is a bound system), the cores will typically pass through one another within $\sim$2 crossings (e.g., Ricker & Sarazin 2001; Poole et al. 2006). The crossing of these two cores will result in both an increase in the effectiveness of ram-pressure stripping, due to the high relative velocities of the cores, and an increased rate of galaxy–galaxy mergers and harassment. Each of these elevated processes result in the removal of cool gas from member galaxy halos. Assuming that this gas remains cool, it would lead to an increase in the availability of fuel for star formation in the cores of merging clusters. This is not the case in low-z systems, however, because galaxies in the cores of low-z clusters tend to be gas-poor (hence the low SFRs), so very little gas is available to be removed from their halos and contributed to the core.

With this scenario in mind, we re-examine Figure 5, modeling the observed evolution in BCG star formation with two distinct evolutionary components. These models, shown in Figure 10, assume that the evolution can be described as the sum of two power laws in time ($\langle \mathrm{sSFR} \rangle \propto e^{t/\tau}$). The best-fitting models have decay times of 4 Gyr (low-z) and 0.7 Gyr (high-z), compared to 1.5 and 2.2 Gyr for high-z cluster and field galaxies, respectively, (Alberts et al. 2014). This model is meant to provide a qualitative assessment of what may be driving star formation in BCGs over time—there is no shortage of models with an equal number of free parameters that would provide an equivalently good fit to these data.

The models shown in Figure 5 were chosen to illustrate two epochs of declining star formation. From $z \sim 1.4$ to $z \sim 0.8$, the sSFR declines more rapidly ($\tau = 0.7$ Gyr) than both the field ($\tau = 2.2$ Gyr) and cluster ($\tau = 1.5$ Gyr) environment, implying that the BCG is quenched more rapidly than the other cluster members. This is consistent with an extrapolation from the field to the cluster environment from Alberts et al. (2014), indicating that (unsurprisingly) quenching of star formation is a strong function of local galaxy density. At late time, from $z \sim 0.6$ to $z \sim 0$, the sSFR of BCGs is evolving more slowly ($\tau = 4$ Gyr) than both the field and cluster environment. Considering that field galaxy evolution is approximately passive, this implies that BCGs have an additional source of fuel—presumably the cooling ICM in relaxed systems. The non-zero slope of this evolution may be due to an ever-improving balance between ICM cooling and AGN feedback in the cores of galaxy clusters, leading to a reduction in the efficiency of ICM cooling over time.

In summary, there appears to be a transition in the source of fuel for star formation in BCGs over the past $\sim$10 Gyr. In nearby clusters, star formation is likely to be fueled by the cooling ICM, and regulated by feedback from the central AGN. At early times, the most star-forming BCGs are found in dynamically unrelaxed clusters, suggesting that star formation may be predominantly fueled by interactions with other galaxies, similar to other, non-BCG members.

4.3. Lowering the Precipitation Threshold in Mergers

Several recent studies have suggested that the condition for thermal instability in the hot ICM can be described as $t_{\rm cool}/t_{\rm ff} = 10$, where $t_{\rm cool}$ is the cooling time and $t_{\rm ff}$ is the local free-fall time (Gaspari et al. 2012; McCourt et al. 2012; Sharma et al. 2012; Gaspari et al. 2015; Voit & Donahue 2015; Voit et al. 2015). This threshold can be interpreted as the ratio of the cooling time to the mixing time. Assuming that AGN feedback is anisotropic, preventing local thermal instabilities requires the heated gas to mix with the cooling gas on timescales shorter than the local cooling time.

In order to cross this threshold, one of two conditions can be met. The gas can cool, reducing the local cooling time, $t_{\rm cool}$. In the precipitation-driven feedback scenario of Voit et al. (2015), this leads to rapid precipitation of cold clouds, which fuel AGN feedback, leading to an increase of $t_{\rm cool}$. This cycle can repeat indefinitely, until a more energetic process drives $t_{\rm cool}$ to much larger values ($\gg$1 Gyr). Alternatively, if the free-fall time is increased, gas at a fixed density and temperature will more readily condense out of the hot phase. This criteria is, in principle, met if the dense core of a galaxy cluster is dislodged from the minimum of the dark matter potential, as is the case during an interaction with another massive group or cluster. It remains unclear, however, whether increasing the free-fall time of the gas in this way would, in fact, lead to more favorable

cooling. Strictly speaking, a dislodged cool core would have a lower value of $t_{\rm cool}/t_{\rm ff}$, but the simulations that arrived at the threshold of $t_{\rm cool}/t_{\rm ff} = 10$ for thermal instability assumed relaxed clusters. In the case of a relaxed cluster, $t_{\rm ff}$ is a proxy for the convective timescale of the hot gas. However, in a merging cluster, bulk flows will likely drive mixing on faster timescales, perhaps leading to *less* efficient cooling.

This represents an alternate scenario that would lead to a link between enhanced star formation in the BCG and an unrelaxed dynamical state of the cluster core at early times. We lean toward the merger-induced SF scenario to explain the uptick in star-forming BCGs at early times, but stress that follow-up studies, including spatially resolved far-UV (e.g., *HST*) and far-IR (e.g., ALMA) imaging and optical spectroscopy, of these BCGs are necessary to provide additional insights into the mechanism for enhancing star formation in these high-z BCGs.

4.4. AGN Contamination

As we discussed in Section 2.6, it is possible that many of the BCGs we have identified as star forming may, instead, be AGN. With the inhomogeneous dataset in hand, it is challenging to differentiate between starburst and AGN, or composite systems, in a uniform way for the full sample. Thus, it may be that both the estimated fraction of star-forming BCGs and the absolute SFRs of these BCGs is biased high.

Considering only clusters at $z > 0.75$ (the two highest redshift bins in Figure 4), we detect star formation in 9–10 out of 22 (41%–45%) BCGs, where the uncertainty represents cases where multiple BCGs were identified in a given cluster. This is a factor of two higher than the fraction of star-forming BCGs at $z \sim 0.4$. If we consider only the subsample of clusters with *HST* follow-up and label systems with symmetric, nuclear UV emission as non-star-forming (see Figures 8 and 9), we find evidence of extended, asymmetric star formation in 4 of 10 (40%) of BCGs. Given the reduction in sample size by requiring *HST* follow-up, the uncertainty on this fraction is larger, with the 95% confidence interval being 16.7%–69.2%. While this is consistent with the observed star-forming fraction of ∼18% at $z \sim 0.4$ (McDonald 2011; Donahue et al. 2015), it is inconsistent with the lower value of ∼5% measured at $z \sim 0$ (Donahue et al. 2010; Fraser-McKelvie et al. 2014). Thus, while we can say with high confidence that the fraction of star-forming BCGs has evolved significantly from $z \sim 0$ to $z \gtrsim 0.4$, our inability to differentiate between central AGN and nuclear starbursts limits our ability to say with certainty whether this fraction continues to grow.

It is important to note, however, that the fraction of nearby BCGs harboring AGN that are bright in the UV or IR continuum is low—the vast majority of cluster-centric AGN are radio galaxies that appear quiescent at most other wavelengths. If the high fraction of systems identified here as star forming are instead AGN, it implies a high accretion rate onto the supermassive black hole at early times (e.g., Russell et al. 2013). Of the hundreds of known BCGs at low-z, only a handful of systems appear to harbor rapidly accreting, radiatively efficient AGN (e.g., Russell et al. 2010; O'Sullivan et al. 2012; Ueda et al. 2013; Kirk et al. 2015; Reynolds et al. 2014; Walker et al. 2014). Thus, we can say with confidence that there is a dramatic increase in the amount of "activity" in BCGs from $z \sim 0$ to $z \sim 1$—whether that activity refers to massive bursts of star formation or the rapid growth of central supermassive black holes remains an open question.

5. SUMMARY

We present multiwavelength observations and inferred SFRs for 90 BCGs in SPT-selected galaxy clusters at $0.25 < z < 1.25$, all of which have archival X-ray data. The main results from this study can be summarized as follows:

1. We find a significant number of BCGs (31/90) with SFR $> 10\ M_\odot\,{\rm yr}^{-1}$, representing a much higher occurrence rate than that observed in galaxy clusters at $z \sim 0$ (∼1%–5%; Donahue et al. 2010; Fraser-McKelvie et al. 2014). Of these 31 BCGs, a quarter (7/31) have SFR $> 100\ M_\odot\,{\rm yr}^{-1}$.
2. The fraction of clusters harboring a star-forming (SFR $> 10\ M_\odot\,{\rm yr}^{-1}$) BCG is found to be ∼20% at $z \sim 0.4$, which is consistent with many earlier works based on optical and X-ray cluster selection. This fraction rises rapidly at $z \gtrsim 0.8$, to a measured value of ∼90% at $z \sim 1.1$.
3. The specific SFR (sSFR $\equiv$ SFR/M_*) of BCGs has evolved more slowly ($\tau = 4$ Gyr) in recent times ($z \lesssim 0.6$) than the overall cluster ($\tau = 1.5$ Gyr) and field ($\tau = 2.2$ Gyr) populations. This is most likely due to a replenishment of gas in the BCG via cooling of the ICM. At early times, the evolution was more rapid ($\tau = 0.7$ Gyr), with the sSFR in BCGs dropping from ∼0.1 Gyr^{-1} at $z = 1.2$ to ∼0.02 Gyr^{-1} at $z = 0.8$.
4. At $z \gtrsim 0.6$ there is no significant correlation between the central entropy of the host cluster and the presence of star-formation signatures in the BCG, contrary to what is observed in nearby clusters.
5. While, at $z \sim 0$, star-forming BCGs are found in the centers of relaxed, cool core clusters, this trend appears to reverse at high-z. At $z \gtrsim 0.6$, the most star-forming BCGs in this sample are found in the cores of morphologically disturbed clusters (based on X-ray asymmetry).
6. Excluding the Phoenix cluster, the most strongly star-forming systems in this sample have SFRs of order ∼100–300 $M_\odot\,{\rm yr}^{-1}$. Based on rest-frame near-UV follow-up of a subsample of high-z systems with *HST*, we find that this star formation can be extended on scales of ∼50–60 kpc.

The observation that an enhancement in BCG star formation correlates to the dynamical state of the cluster at high-z suggests that star formation may have been fueled by interactions with gas-rich satellites at early times. Further studies utilizing deep, high angular resolution far-IR and far-UV imaging and integral field spectroscopy of a larger sample of BCGs will help determine if such mergers are, indeed, the dominant source of star formation in BCGs at early times.

We thank Mark Voit and John ZuHone for helpful conversations. M.M. acknowledges support by NASA through contracts HST-GO-13456.002A (Hubble) and GO4-15122A (Chandra), and Hubble Fellowship grant HST-HF51308.01-A awarded by the Space Telescope Science Institute, which is operated by the Association of Universities for Research in Astronomy, Inc., for NASA, under contract NAS 5-26555. The South Pole Telescope program is supported by the National Science Foundation through grants ANT-0638937 and PLR-1248097. Partial support is also provided by the NSF Physics Frontier Center grant PHY-0114422 to the Kavli Institute of Cosmological Physics at the University of Chicago, the Kavli Foundation, and the Gordon and Betty Moore Foundation. Support for X-ray analysis was provided by NASA through

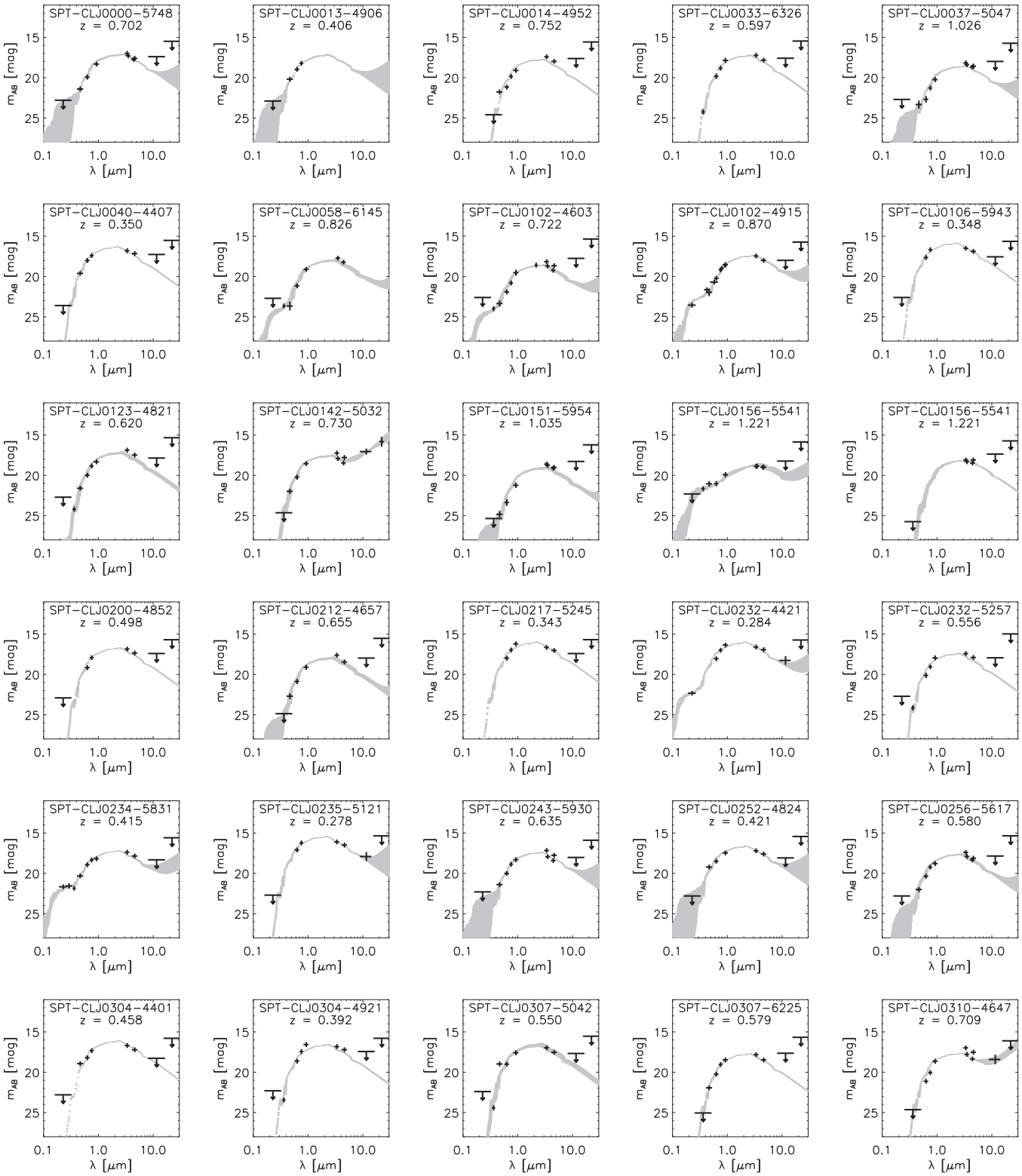

Figure 11. Broadband spectral energy distribution for 90 BCGs in this sample. Wavelengths here are in the observed frame. We overplot the best-fitting models from 100 fits, while varying unknown quantities such as the intrinsic reddening ($E(B-V) = 0.3 \pm 0.1$), the mid-IR slope ($\alpha = 2.0 \pm 0.5$), and the formation epoch of the old population ($z_f = 2$–5). The model consists of an old stellar population, formed at $z = z_f$ (Leitherer et al. 1999), a young stellar population that has been continuously forming stars for 30 Myr (Leitherer et al. 1999), and a dust component parametrized by a power law in the mid-IR, following Casey (2012).

Chandra Award Numbers 12800071, 12800088, and 13800883 issued by the Chandra X-ray Observatory Center, which is operated by the Smithsonian Astrophysical Observatory for and on behalf of NASA. Galaxy cluster research at Harvard is supported by NSF grant AST-1009012 and at SAO by NSF grants AST-1009649 and MRI-0723073. The McGill group acknowledges funding from the National Sciences and Engineering Research Council of Canada, Canada Research

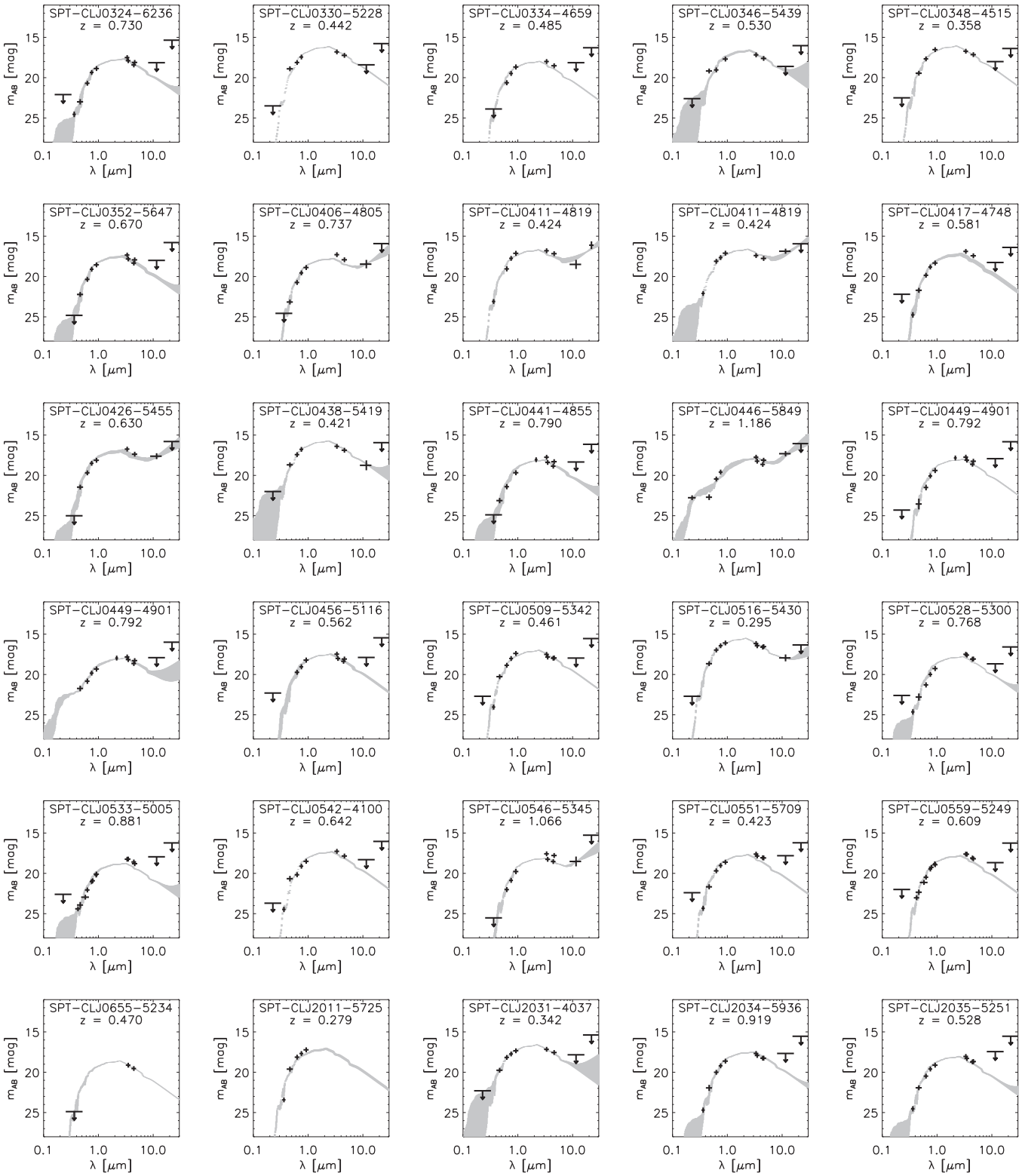

Figure 11. (Continued.)

Chairs program, and the Canadian Institute for Advanced Research. Argonne National Laboratory's work was supported under U.S. Department of Energy contract DE-AC02-06CH11357. This work is based in part on observations made with the *Spitzer Space Telescope*, which is operated by the Jet Propulsion Laboratory, California Institute of Technology under a contract with NASA. J.E.C. acknowledges support from National Science Foundation grants PLR-1248097 and PHY-1125897. C.R. acknowledges support from the University of Melbourne and from the Australian Research Councils

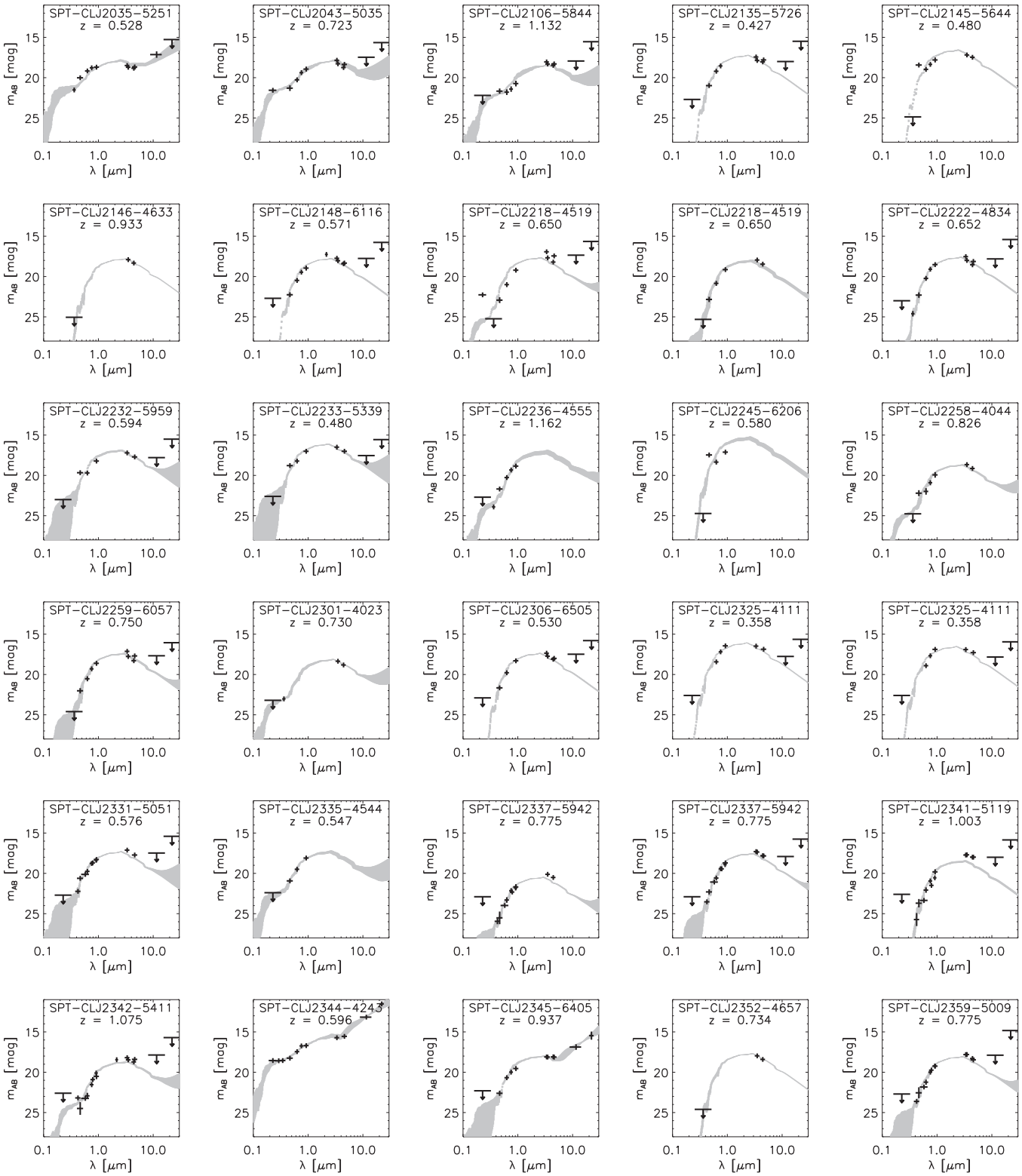

Figure 11. (Continued.)

Discovery Projects scheme (DP150103208). D.A. and T.S. acknowledge support from the German Federal Ministry of Economics and Technology (BMWi) provided through DLR under projects 50 OR 1210, 50 OR 1308, and 50 OR 1407.

Facilities: Blanco (MOSAIC), CXO (ACIS), *GALEX*, *HST* (ACS), *Magellan:* Baade (FourStar, IMACS), *Magellan:* Clay (LDSS3, Megacam), Max Planck:2.2m (WFI), NTT (EFOSC), *Spitzer* (IRAC), Swope (SITe3), VLT:Antu (FORS2), *WISE*, XMM (OM).

Table 2
BCG Star Formation Rates and Stellar Masses

Cluster	$z_{\rm cluster}$	$\alpha_{\rm BCG}$ (°)	$\delta_{\rm BCG}$ (°)	M_* ($10^{12} M_\odot$)	SFR$_{\rm UV}$ ($M_\odot$ yr^{-1})	SFR$_{\rm [O\ II]}$ ($M_\odot$ yr^{-1})	SFR$_{24\ \mu m}$ ($M_\odot$ yr^{-1})
SPT-CLJ0000-5748	0.702	0.2501	−57.8093	$2.54^{+0.17}_{-0.23}$	52^{+89}_{-39}	51^{+28}_{-20}	<85
SPT-CLJ0013-4906	0.406	3.3306	−49.1099	$0.98^{+0.12}_{-0.10}$	<50	<8.6	⋯
SPT-CLJ0014-4952	0.752	3.7041	−49.8851	$1.68^{+0.10}_{-0.29}$	<10.	⋯	<92
SPT-CLJ0033-6326	0.597	8.4710	−63.4449	$2.45^{+0.09}_{-0.18}$	<1300	<12	<43
SPT-CLJ0037-5047	1.026	9.4478	−50.7890	$1.00^{+0.12}_{-0.18}$	21^{+40}_{-15}	<14	<170
SPT-CLJ0040-4407	0.350	10.2080	−44.1307	$1.79^{+0.26}_{-0.11}$	<8.5	⋯	<14
SPT-CLJ0058-6145	0.826	14.5842	−61.7669	$1.54^{+0.49}_{-0.47}$	24^{+34}_{-13}	⋯	⋯
SPT-CLJ0102-4603	0.722	15.6779	−46.0710	$0.73^{+0.22}_{-0.16}$	$15^{+20}_{-9.0}$	⋯	<79
SPT- CLJ0102-4915	0.870	15.7407	−49.2720	$2.43^{+0.24}_{-0.39}$	93^{+120}_{-55}	⋯	<88
SPT-CLJ0106-5943	0.348	16.6197	−59.7201	$3.38^{+0.18}_{-0.23}$	<20	<5.1	<7.3
SPT-CLJ0123-4821	0.620	20.7956	−48.3563	$2.09^{+0.75}_{-0.64}$	<3.6	⋯	<39
SPT-CLJ0142-5032	0.730	25.5401	−50.5410	$1.39^{+0.48}_{-0.18}$	<7.7	⋯	92^{+54}_{-34}
SPT-CLJ0151-5954	1.035	27.8634	−59.9062	$0.63^{+0.28}_{-0.11}$	<6.4	⋯	<140
SPT-CLJ0156-5541	1.221	29.0436	−55.6985	$0.33^{+0.34}_{-0.29}$	400^{+410}_{-220}	⋯	<210
SPT-CLJ0156-5541	1.221	29.0382	−55.7029	$1.79^{+0.25}_{-0.45}$	<9.0	⋯	<530
SPT-CLJ0200-4852	0.498	30.1421	−48.8712	$3.12^{+0.03}_{-0.22}$	<34	<26	<29
SPT-CLJ0212-4657	0.655	33.0986	−46.9537	$1.47^{+0.09}_{-0.46}$	<1.0	⋯	<49
SPT-CLJ0217-5245	0.343	34.3122	−52.7604	$2.88^{+0.17}_{-0.07}$	<450	⋯	<9.2
SPT-CLJ0232-4421	0.284	38.0773	−44.3467	$2.07^{+0.12}_{-0.16}$	$17^{+19}_{-10.0}$	⋯	<11
SPT-CLJ0232-5257	0.556	38.2058	−52.9531	$1.85^{+0.11}_{-0.07}$	<1.1	⋯	<26
SPT-CLJ0234-5831	0.415	38.6761	−58.5236	$0.94^{+0.09}_{-0.11}$	50^{+71}_{-28}	59^{+35}_{-22}	<7.0
SPT-CLJ0235-5121	0.278	38.9387	−51.3512	$3.45^{+0.03}_{-0.33}$	<13	⋯	<14
SPT-CLJ0243-5930	0.635	40.8628	−59.5172	$1.67^{+0.09}_{-0.14}$	<100	<10.	<35
SPT-CLJ0252-4824	0.421	43.2083	−48.4162	$1.24^{+0.14}_{-0.10}$	<59	<26	<5.9
SPT-CLJ0256-5617	0.580	44.1056	−56.2978	$1.45^{+0.26}_{-0.50}$	<11	⋯	<35
SPT-CLJ0304-4401	0.458	46.0707	−44.0256	$3.22^{+0.27}_{-0.04}$	<30	<17	<6.1
SPT-CLJ0304-4921	0.392	46.0673	−49.3571	$2.14^{+0.27}_{-0.17}$	<35	⋯	<15
SPT-CLJ0307-5042	0.550	46.9605	−50.7012	$1.97^{+2.34}_{-0.15}$	<64	⋯	<25
SPT-CLJ0307-6225	0.579	46.8195	−62.4465	$1.12^{+0.08}_{-0.08}$	<4.0	<14	<44
SPT-CLJ0310-4647	0.709	47.6354	−46.7856	$2.19^{+0.08}_{-0.21}$	<8.3	<11	34^{+21}_{-13}
SPT-CLJ0324-6236	0.730	51.0511	−62.5988	$1.73^{+0.29}_{-0.21}$	<13	⋯	<57
SPT-CLJ0330-5228	0.442	52.7374	−52.4704	$2.99^{+0.13}_{-0.23}$	<15	⋯	<4.8
SPT-CLJ0334-4659	0.485	53.5457	−46.9958	$0.93^{+0.02}_{-0.07}$	<8.7	79^{+45}_{-30}	<18
SPT-CLJ0346-5439	0.530	56.7308	−54.6487	$2.41^{+0.28}_{-0.22}$	<120	⋯	<5.7
SPT-CLJ0348-4515	0.358	57.0719	−45.2498	$2.32^{+0.00}_{-0.17}$	<22	<4.7	<5.7
SPT-CLJ0352-5647	0.670	58.2397	−56.7977	$1.93^{+0.21}_{-0.38}$	<6.8	⋯	<50
SPT-CLJ0406-4805	0.737	61.7302	−48.0826	$1.57^{+0.10}_{-0.24}$	<10.0	<21	41^{+26}_{-16}
SPT-CLJ0411-4819	0.424	62.7957	−48.3277	$2.17^{+0.16}_{-0.14}$	⋯	<5.5	$15^{+4.4}_{-4.4}$
SPT-CLJ0411-4819	0.424	62.8154	−48.3175	$2.54^{+0.07}_{-0.21}$	<12	⋯	$27^{+5.0}_{-11}$
SPT-CLJ0417-4748	0.581	64.3461	−47.8132	$2.33^{+0.23}_{-0.63}$	<93	<3.8	<28
SPT-CLJ0426-5455	0.630	66.5171	−54.9253	$2.89^{+0.67}_{-1.20}$	<4.7	⋯	51^{+41}_{-22}
SPT-CLJ0438-5419	0.421	69.5734	−54.3224	$3.98^{+0.25}_{-0.20}$	<31	<23	<24
SPT-CLJ0441-4855	0.790	70.4497	−48.9233	$1.38^{+0.17}_{-0.23}$	<13	⋯	<61
SPT-CLJ0446-5849	1.186	71.5157	−58.8304	$1.46^{+0.39}_{-0.59}$	200^{+450}_{-140}	⋯	330^{+270}_{-170}
SPT-CLJ0449-4901	0.792	72.2819	−49.0214	$1.36^{+0.04}_{-0.19}$	<10.	⋯	<84
SPT- CLJ0449-4901	0.792	72.2669	−49.0276	$1.21^{+0.14}_{-0.22}$	88^{+110}_{-47}	<27	<81
SPT-CLJ0456-5116	0.562	74.1171	−51.2764	$1.48^{+0.13}_{-0.34}$	<79	<6.3	<32
SPT-CLJ0509-5342	0.461	77.3393	−53.7035	$1.54^{+0.11}_{-0.16}$	<32	33^{+20}_{-12}	<16
SPT-CLJ0516-5430	0.295	79.1556	−54.5004	$2.90^{+0.18}_{-0.17}$	<13	<27	$2.5^{+1.3}_{-0.82}$
SPT-CLJ0528-5300	0.768	82.0222	−52.9981	$1.59^{+0.05}_{-0.13}$	<10.	<15	<34
SPT-CLJ0533-5005	0.881	83.4033	−50.0958	$0.75^{+0.03}_{-0.08}$	<16	50^{+29}_{-19}	<130
SPT-CLJ0542-4100	0.642	85.7085	−41.0001	$1.86^{+0.11}_{-0.16}$	<1.4	⋯	<28
SPT-CLJ0546-5345	1.066	86.6573	−53.7588	$1.70^{+0.09}_{-0.30}$	<8.0	⋯	110^{+89}_{-53}
SPT-CLJ0551-5709	0.423	87.8931	−57.1451	$0.69^{+0.06}_{-0.02}$	<37	⋯	<17
SPT-CLJ0559-5249	0.609	89.9301	−52.8242	$1.11^{+0.10}_{-0.11}$	<11	<16	<19
SPT-CLJ0655-5234	0.470	103.9760	−52.5674	$0.36^{+0.00}_{-0.02}$	<3.1	⋯	⋯
SPT-CLJ2011-5725	0.279	302.8620	−57.4196	$0.71^{+0.02}_{-0.10}$	⋯	⋯	⋯

Table 2
(Continued)

Cluster	$z_{\rm cluster}$	$\alpha_{\rm BCG}$ (°)	$\delta_{\rm BCG}$ (°)	M_* ($10^{12}M_\odot$)	SFR$_{\rm UV}$ ($M_\odot$ yr^{-1})	SFR$_{\rm [O\ II]}$ ($M_\odot$ yr^{-1})	SFR $_{24\ \mu m}$ ($M_\odot$ yr^{-1})
SPT-CLJ2031-4037	0.342	307.9720	−40.6252	$1.33^{+0.02}_{-0.15}$	<51	⋯	<7.5
SPT-CLJ2034-5936	0.919	308.5390	−59.6042	$1.97^{+0.18}_{-0.30}$	<4.5	⋯	<99
SPT-CLJ2035-5251	0.528	308.7950	−52.8564	$0.72^{+0.05}_{-0.01}$	<2.8	<2.4	<41
SPT-CLJ2035-5251	0.528	308.7930	−52.8539	$0.55^{+0.08}_{-0.05}$	120^{+78}_{-60}	⋯	31^{+29}_{-16}
SPT-CLJ2043-5035	0.723	310.8230	−50.5923	$0.88^{+0.26}_{-0.37}$	210^{+240}_{-130}	110^{+54}_{-47}	<89
SPT-CLJ2106-5844	1.132	316.5190	−58.7411	$0.83^{+0.28}_{-0.27}$	200^{+240}_{-110}	⋯	<260
SPT-CLJ2135-5726	0.427	323.9060	−57.4418	$1.07^{+0.08}_{-0.03}$	<13	<8.5	<13
SPT-CLJ2145-5644	0.480	326.4660	−56.7482	$2.30^{+0.05}_{-0.13}$	<3.6	<26	⋯
SPT-CLJ2146-4633	0.933	326.6470	−46.5505	$1.96^{+0.04}_{-0.25}$	<9.6	<34	⋯
SPT-CLJ2148-6116	0.571	327.1780	−61.2795	$1.04^{+0.07}_{-0.05}$	<7.5	⋯	<39
SPT-CLJ2218-4519	0.650	334.7470	−45.3145	$1.12^{+0.03}_{-0.09}$	$4.4^{+5.0}_{-2.4}$	⋯	<55
SPT-CLJ2218-4519	0.650	334.7500	−45.3162	$1.06^{+0.25}_{-0.27}$	<1.0	⋯	⋯
SPT-CLJ2222-4834	0.652	335.7110	−48.5764	$1.47^{+0.05}_{-0.08}$	<3.1	⋯	<52
SPT-CLJ2232-5959	0.594	338.1410	−59.9980	$2.27^{+0.38}_{-0.26}$	<110	<18	<33
SPT-CLJ2233-5339	0.480	338.3150	−53.6526	$2.58^{+0.27}_{-0.20}$	<86	<12	<13
SPT-CLJ2236-4555	1.162	339.2140	−45.9295	$3.29^{+0.64}_{-0.97}$	50^{+69}_{-30}	⋯	⋯
SPT-CLJ2245-6206	0.580	341.2590	−62.1272	$7.09^{+4.64}_{-0.86}$	<5.2	⋯	⋯
SPT-CLJ2258-4044	0.826	344.7010	−40.7418	$0.62^{+0.08}_{-0.07}$	$10.^{+12}_{-5.7}$	⋯	⋯
SPT-CLJ2259-6057	0.750	344.7540	−60.9595	$2.15^{+0.44}_{-0.25}$	<11	⋯	<84
SPT-CLJ2301-4023	0.730	345.4700	−40.3868	$1.04^{+0.07}_{-0.15}$	36^{+53}_{-19}	⋯	⋯
SPT-CLJ2306-6505	0.530	346.7230	−65.0882	$1.34^{+0.06}_{-0.05}$	<14	<2.6	<39
SPT-CLJ2325-4111	0.358	351.2990	−41.2037	$3.01^{+0.10}_{-0.13}$	<9.8	<11	<6.7
SPT-CLJ2325-4111	0.358	351.3000	−41.1991	$1.96^{+0.26}_{-0.03}$	<14	<5.0	<8.4
SPT-CLJ2331-5051	0.576	352.9630	−50.8650	$1.53^{+0.06}_{-0.08}$	23^{+36}_{-14}	⋯	<46
SPT-CLJ2335-4544	0.547	353.7850	−45.7391	$1.40^{+0.22}_{-0.37}$	41^{+61}_{-27}	<6.7	⋯
SPT-CLJ2337-5942	0.775	354.3550	−59.7058	$0.13^{+0.01}_{-0.01}$	$1.00^{+1.5}_{-0.66}$	⋯	⋯
SPT-CLJ2337-5942	0.775	354.3650	−59.7013	$2.08^{+0.09}_{-0.28}$	<4.9	<40	<76
SPT-CLJ2341-5119	1.003	355.3010	−51.3291	$1.15^{+0.10}_{-0.25}$	<2.5	⋯	<170
SPT-CLJ2342-5411	1.075	355.6910	−54.1847	$0.90^{+0.13}_{-0.22}$	33^{+42}_{-19}	<17	<240
SPT-CLJ2344-4243	0.596	356.1830	−42.7201	$3.95^{+1.85}_{-2.43}$	2000^{+2400}_{-1200}	1700^{+1100}_{-710}	2000^{+860}_{-730}
SPT-CLJ2345-6405	0.937	356.2510	−64.0927	$1.20^{+0.11}_{-0.16}$	<71	⋯	250^{+130}_{-89}
SPT-CLJ2352-4657	0.734	358.0680	−46.9602	$1.64^{+0.07}_{-0.14}$	<9.5	⋯	⋯
SPT-CLJ2359-5009	0.775	359.9280	−50.1672	$1.25^{+0.05}_{-0.15}$	$8.2^{+13}_{-6.0}$	<21	<84

Note. Positions and star-formation rates of BCGs used in this study. UV- and [O II]-derived SFRs are corrected for intrinsic extinction assuming $E(B-V) = 0.3 \pm 0.1$ and a gray extinction curve from Calzetti et al. (2000). Systematic uncertainties, which are dominated by the extinction correction in the blue bands and extrapolation to 24 μm in the IR band, are quoted for all detections. These uncertainties are discussed in detail in Section 2.5.

APPENDIX
SPECTRAL ENERGY DISTRIBUTIONS

Below, we provide the spectral energy distribution for each galaxy in our sample (Figure 11). For each galaxy we show the best-fit model overlaid on the data. Following these figures, we provide a table (Table 2) with the derived parameters from this best-fit model.

REFERENCES

Alberts, S., Pope, A., Brodwin, M., et al. 2014, MNRAS, 437, 437
Balogh, M. L., Morris, S. L., Yee, H. K. C., Carlberg, R. G., & Ellingson, E. 1999, ApJ, 527, 54
Bertin, E., & Arnouts, S. 1996, A&AS, 117, 393
Bîrzan, L., Rafferty, D. A., McNamara, B. R., Wise, M. W., & Nulsen, P. E. J. 2004, ApJ, 607, 800
Bleem, L. E., Stalder, B., de Haan, T., et al. 2015, ApJS, 216, 27
Brodwin, M., Stanford, S. A., Gonzalez, A. H., et al. 2013, ApJ, 779, 138
Butcher, H., & Oemler, A., Jr. 1984, ApJ, 285, 426
Calzetti, D. 2001, PASP, 113, 1449
Calzetti, D., Armus, L., Bohlin, R. C., et al. 2000, ApJ, 533, 682
Calzetti, D., Kennicutt, R. C., Engelbracht, C. W., et al. 2007, ApJ, 666, 870
Cameron, E. 2011, PASA, 28, 128
Canning, R. E. A., Ryon, J. E., Gallagher, J. S., et al. 2014, MNRAS, 444, 336
Carlstrom, J. E., Ade, P. A. R., Aird, K. A., et al. 2011, PASP, 123, 568
Casey, C. M. 2012, MNRAS, 425, 3094
Cavagnolo, K. W., Donahue, M., Voit, G. M., & Sun, M. 2008, ApJL, 683, L107
Cavagnolo, K. W., Donahue, M., Voit, G. M., & Sun, M. 2009, ApJS, 182, 12
Conselice, C. J., Gallagher, J. S., III, & Wyse, R. F. G. 2001, AJ, 122, 2281
Crawford, C. S., Allen, S. W., Ebeling, H., Edge, A. C., & Fabian, A. C. 1999, MNRAS, 306, 857
Donahue, M., Bruch, S., Wang, E., et al. 2010, ApJ, 715, 881
Donahue, M., Connor, T., Fogarty, K., et al. 2015, ApJ, 805, 177
Donahue, M., Mack, J., Voit, G. M., et al. 2000, ApJ, 545, 670
Donahue, M., Stocke, J. T., & Gioia, I. M. 1992, ApJ, 385, 49
Dressler, A., Bigelow, B., Hare, T., et al. 2011, PASP, 123, 288
Edge, A. C. 2001, MNRAS, 328, 762
Edge, A. C., & Frayer, D. T. 2003, ApJL, 594, L13
Edge, A. C., Wilman, R. J., Johnstone, R. M., et al. 2002, MNRAS, 337, 49
Edwards, L. O. V., Hudson, M. J., Balogh, M. L., & Smith, R. J. 2007, MNRAS, 379, 100
Ehlert, S., Allen, S. W., von der Linden, A., et al. 2011, MNRAS, 411, 1641
Fabian, A. C. 2012, ARA&A, 50, 455

Förster Schreiber, N. M., Genzel, R., Lutz, D., & Sternberg, A. 2003, ApJ, 599, 193
Fraser-McKelvie, A., Brown, M. J. I., & Pimbblet, K. A. 2014, MNRAS, 444, L63
Gaspari, M., Brighenti, F., & Temi, P. 2015, A&A, 579, A62
Gaspari, M., Ruszkowski, M., & Sharma, P. 2012, ApJ, 746, 94
Haarsma, D. B., Leisman, L., Donahue, M., et al. 2010, ApJ, 713, 1037
Hatch, N. A., Crawford, C. S., & Fabian, A. C. 2007, MNRAS, 380, 33
Hatch, N. A., Crawford, C. S., Fabian, A. C., & Johnstone, R. M. 2005, MNRAS, 358, 765
Heckman, T. M., Baum, S. A., van Breugel, W. J. M., & McCarthy, P. 1989, ApJ, 338, 48
Hicks, A. K., & Mushotzky, R. 2005, ApJL, 635, L9
Hicks, A. K., Mushotzky, R., & Donahue, M. 2010, ApJ, 719, 1844
Hlavacek-Larrondo, J., Fabian, A. C., Edge, A. C., et al. 2012, MNRAS, 421, 1360
Hlavacek-Larrondo, J., McDonald, M., Benson, B. A., et al. 2015, ApJ, 805, 35
Hoffer, A. S., Donahue, M., Hicks, A., & Barthelemy, R. S. 2012, ApJS, 199, 23
Hu, E. M., Cowie, L. L., & Wang, Z. 1985, ApJS, 59, 447
Hudson, D. S., Mittal, R., Reiprich, T. H., et al. 2010, A&A, 513, A37
Jaffe, W., & Bremer, M. N. 1997, MNRAS, 284, L1
Jaffe, W., Bremer, M. N., & Baker, K. 2005, MNRAS, 360, 748
Johnstone, R. M., Fabian, A. C., & Nulsen, P. E. J. 1987, MNRAS, 224, 75
Johnstone, R. M., Hatch, N. A., Ferland, G. J., et al. 2007, MNRAS, 382, 1246
Kewley, L. J., Geller, M. J., & Jansen, R. A. 2004, AJ, 127, 2002
Kirk, B., Hilton, M., Cress, C., et al. 2015, MNRAS, 449, 4010
Leitherer, C., Schaerer, D., Goldader, J. D., et al. 1999, ApJS, 123, 3
Mantz, A. B., Allen, S. W., Morris, R. G., et al. 2015, MNRAS, 449, 199
McCourt, M., Sharma, P., Quataert, E., & Parrish, I. J. 2012, MNRAS, 419, 3319
McDonald, M. 2011, ApJL, 742, L35
McDonald, M., Bayliss, M., Benson, B. A., et al. 2012a, Natur, 488, 349
McDonald, M., Benson, B., Veilleux, S., Bautz, M. W., & Reichardt, C. L. 2013a, ApJL, 765, L37
McDonald, M., Benson, B. A., Vikhlinin, A., et al. 2013b, ApJ, 774, 23
McDonald, M., Benson, B. A., Vikhlinin, A., et al. 2014a, ApJ, 794, 67
McDonald, M., Roediger, J., Veilleux, S., & Ehlert, S. 2014b, ApJL, 791, L30
McDonald, M., Swinbank, M., Edge, A. C., et al. 2014c, ApJ, 784, 18
McDonald, M., & Veilleux, S. 2009, ApJL, 703, L172
McDonald, M., Veilleux, S., & Mushotzky, R. 2011a, ApJ, 731, 33
McDonald, M., Veilleux, S., & Rupke, D. S. N. 2012b, ApJ, 746, 153
McDonald, M., Veilleux, S., Rupke, D. S. N., & Mushotzky, R. 2010, ApJ, 721, 1262
McDonald, M., Veilleux, S., Rupke, D. S. N., Mushotzky, R., & Reynolds, C. 2011b, ApJ, 734, 95
McDonald, M., Wei, L. H., & Veilleux, S. 2012c, ApJL, 755, L24
McLeod, B., Geary, J., Conroy, M., et al. 2015, PASP, 127, 366
McNamara, B. R., & Nulsen, P. E. J. 2012, NJPh, 14, 055023
McNamara, B. R., & O'Connell, R. W. 1989, AJ, 98, 2018
McNamara, B. R., Rafferty, D. A., Bîrzan, L., et al. 2006, ApJ, 648, 164
Morrissey, P., Conrow, T., Barlow, T. A., et al. 2007, ApJS, 173, 682
Nurgaliev, D., McDonald, M., Benson, B. A., et al. 2013, ApJ, 779, 112
O'Dea, C. P., Baum, S. A., Privon, G., et al. 2008, ApJ, 681, 1035
O'Dea, K. P., Quillen, A. C., O'Dea, C. P., et al. 2010, ApJ, 719, 1619
Ogrean, G. A., Hatch, N. A., Simionescu, A., et al. 2010, MNRAS, 406, 354
Oonk, J. B. R., Jaffe, W., Bremer, M. N., & van Weeren, R. J. 2010, MNRAS, 405, 898
O'Sullivan, E., Giacintucci, S., Babul, A., et al. 2012, MNRAS, 424, 2971
Panagoulia, E. K., Fabian, A. C., & Sanders, J. S. 2014, MNRAS, 438, 2341
Poole, G. B., Fardal, M. A., Babul, A., et al. 2006, MNRAS, 373, 881
Pratt, G. W., Croston, J. H., Arnaud, M., & Böhringer, H. 2009, A&A, 498, 361
Price, S. D., Paxson, C., Engelke, C., & Murdock, T. L. 2004, AJ, 128, 889
Rafferty, D. A., McNamara, B. R., & Nulsen, P. E. J. 2008, ApJ, 687, 899
Rawle, T. D., Edge, A. C., Egami, E., et al. 2012, ApJ, 747, 29
Reynolds, C. S., Lohfink, A. M., Babul, A., et al. 2014, ApJL, 792, L41
Ricker, P. M., & Sarazin, C. L. 2001, ApJ, 561, 621
Ruel, J., Bazin, G., Bayliss, M., et al. 2014, ApJ, 792, 45
Russell, H. R., Fabian, A. C., Sanders, J. S., et al. 2010, MNRAS, 402, 1561
Russell, H. R., McNamara, B. R., Edge, A. C., et al. 2013, MNRAS, 432, 530
Ruszkowski, M., & Springel, V. 2009, ApJ, 696, 1094
Salomé, P., & Combes, F. 2003, A&A, 412, 657
Salpeter, E. E. 1955, ApJ, 121, 161
Santos, J. S., Rosati, P., Tozzi, P., et al. 2008, A&A, 483, 35
Sharma, P., McCourt, M., Quataert, E., & Parrish, I. J. 2012, MNRAS, 420, 3174
Sharma, P., Parrish, I. J., & Quataert, E. 2010, ApJ, 720, 652
Shull, J. M., Smith, B. D., & Danforth, C. W. 2012, ApJ, 759, 23
Silk, J., & Mamon, G. A. 2012, RAA, 12, 917
Song, J., Zenteno, A., Stalder, B., et al. 2012, ApJ, 761, 22
Stern, D., Assef, R. J., Benford, D. J., et al. 2012, ApJ, 753, 30
Stern, D., Eisenhardt, P., Gorjian, V., et al. 2005, ApJ, 631, 163
Sun, M. 2009, ApJ, 704, 1586
Sunyaev, R. A., & Zeldovich, Y. B. 1972, CoASP, 4, 173
Tremblay, G. R., O'Dea, C. P., Baum, S. A., et al. 2012, MNRAS, 424, 1042
Tremblay, G. R., O'Dea, C. P., Baum, S. A., et al. 2015, MNRAS, 451, 3768
Ueda, S., Hayashida, K., Anabuki, N., et al. 2013, ApJ, 778, 33
Vikhlinin, A., Burenin, R., Forman, W. R., et al. 2007, in Heating versus Cooling in Galaxies and Clusters of Galaxies, ed. H. Böhringer et al., 48
Vikhlinin, A., Burenin, R. A., Ebeling, H., et al. 2009, ApJ, 692, 1033
Vikhlinin, A., Kravtsov, A., Forman, W., et al. 2006, ApJ, 640, 691
Voigt, L. M., & Fabian, A. C. 2004, MNRAS, 347, 1130
Voit, G. M., & Donahue, M. 2015, ApJL, 799, L1
Voit, G. M., Donahue, M., Bryan, G. L., & McDonald, M. 2015, Natur, 519, 203
Wagner, C. R., Brodwin, M., Snyder, G. F., et al. 2015, ApJ, 800, 107
Walker, S. A., Fabian, A. C., Russell, H. R., & Sanders, J. S. 2014, MNRAS, 442, 2809
Wright, E. L., Eisenhardt, P. R. M., Mainzer, A. K., et al. 2010, AJ, 140, 1868